Applicability of numerical water tank for the dynamic response analysis of the barge-type floating platform

Otori, Hiromasa; Kikuchi, Yuka; Rivera-Arreba, Irene; Viré, Axelle

DOI
10.1016/j.oceaneng.2024.118915

Publication date
2024

Document Version
Final published version

Published in
Ocean Engineering

Ocean Engineering 312 (2024) 118915

Contents lists available at ScienceDirect

Ocean Engineering

journal homepage: www.elsevier.com/locate/oceaneng

Research paper

Applicability of numerical water tank for the dynamic response analysis of the barge-type floating platform

Hiromasa Otori [a], Yuka Kikuchi [a,*], Irene Rivera-Arreba [b], Axelle Viré [c]

[a] Department of Civil Engineering, School of Engineering, The University of Tokyo, 7-3-1 Hongo, Bunkyo-ku, Tokyo, Japan
[b] Department of Marine Technology, Norwegian University of Science and Technology, Høgskoleringen 1, 7034, Trondheim, Norway
[c] Wind Energy Section, Delft University of Technology, 2629 HS, Delft, the Netherlands

ARTICLE INFO

Keywords:
Barge-type floater
Computational fluid dynamics
Dynamic analysis
Wave drift force
Drag coefficient model
The coupling of surge and pitch

ABSTRACT

A fully nonlinear Navier-Stokes/VOF numerical water tank is developed for barge-type floaters with coupling to the dynamic mooring line model. Wave excitation forces, free decay responses, and dynamic responses in regular waves predicted by numerical water tank show good agreement with experimental results. Then, hydrodynamic force models used in engineering models are improved by applying the numerical water tank results. It is clarified that the cause of the overestimation of normalized wave excitation force at water tank test relative to that predicted by potential theory is the underestimation of the input wave height due to the interference of the reflected wave from the floater. The new drag coefficient model is proposed based on numerical forced oscillation simulations at the surge natural period. The wave drift QTF is evaluated using the numerical water tank and the prediction accuracy of the mean floater displacement in the surge direction is improved, compared to the conventional Newman's approximation model. The surge-pitch coupling terms of drag force and its mechanism are investigated by forced oscillation simulations. The correction method of surge-pitch coupling terms of drag force is proposed and the prediction accuracy of the floater displacement in the surge direction is improved.

1. Introduction

Floating offshore wind turbines (FOWTs) are a promising technology for harnessing the vast potential of offshore wind energy in deep ocean regions to generate power. Many demonstration projects have been conducted over the world (Hywind Demo, 2009; WindFloat 1, 2009; Fukushima, 2013; Goto Island project, 2013 (Utsunomiya, 2016)). In various floater types, the shallow drafted barge-type floater is expected as a low-cost platform suitable for water depths of 50–100 m. In 2018, a 2 MW barge-type FOWT was installed in the FLOATGEN project in France (FLOATGEN, 2018) and a 3 MW one in NEDO Demonstration Project of Next-Generation Offshore Floating Wind Turbine in Japan (NEDO Demonstration Project of Next-Generation Offshore Floating Wind Turbine, 2019). Barge-type floaters typically show larger pitch motions compared to spar and semi-submersible type floaters. The natural period of barge-type floaters in the pitch direction typically fall within a similar range to dominant wave periods, while those of spar-type and semi-submersible type floaters are longer periods (Jonkman, 2007; Kikuchi and Ishihara, 2020). Skirts are used for the platforms in the demonstration projects (FLOATGEN, 2018; NEDO Demonstration Project of Next-Generation Offshore Floating Wind Turbine, 2019) to suppress the dynamic responses of floaters, which generate strong nonlinear drag forces.

Numerical modeling techniques for floating offshore wind turbine systems are categorized into three levels: low-, mid-, and high-fidelity (Otter et al., 2021). Mid-fidelity models, often referred to as engineering-level model or engineering model, are commonly used for dynamic analysis based on the equations of motion employing potential-flow theory and Morison's equation. Engineering models are suitable for the design of floating offshore wind turbine system. High-fidelity models, such as computational fluid dynamics (CFD) are used for detailed investigations of local flow phenomena. In the comprehensive benchmark study to date named the Offshore Code Comparison Collaboration projects (OC3 – OC7), a three-way validation has been conducted among engineering models, high-fidelity models, and measurements from water tank tests for semi-submersible type floaters (Benitz et al., 2014; Robertson and Wang, 2021). It is said that the CFD simulations can be used as references for tuning the mid-fidelity engineering-level tools and enable expedient and nonintrusive extraction of flow-field variables and flow visualizations, which are critical to

* Corresponding author.
E-mail address: kikuchi@bridge.t.u-tokyo.ac.jp (Y. Kikuchi).

https://doi.org/10.1016/j.oceaneng.2024.118915
Received 17 May 2024; Received in revised form 26 July 2024; Accepted 3 August 2024
Available online 19 September 2024

obtaining a better understanding of the underprediction issue and possibly lead to improvements to the model formulation and modeling practices used by the mid-fidelity engineering design tools (Wang et al., 2021). The findings in high-fidelity models have been feedbacked to engineering models and the prediction accuracy of engineering model has been improved. For example, advanced hydrodynamic force models were developed based on the forced oscillation simulations using CFD and the prediction accuracy of floater motions using engineering model was improved (Zhang and Ishihara, 2018; Ishihara and Liu, 2020; Otori et al., 2023).

In high-fidelity models, numerical forced oscillation simulations have been validated for barge-type floaters (Otori et al., 2023). Recently, numerical water tanks coupling equation of motion and Navier-Stokes equation have been developed, and the effect of the nonlinear hydrodynamic forces on floater motions has been investigated. The floater motions for OC3 Hywind platform model were analyzed in the previous studies using CFD to consider the nonlinear hydrodynamic forces (Beyer et al., 2013). For more complex structure, the semi-submersible platform model was considered in OC4 projects and the floater motions were analyzed (Benitz et al., 2014; Tran and Kim, 2015, 2016). Rivera-Arreba et al. (2019) investigated the effect of the nonlinearities in the severe waves on semi-submersible type floater responses. For the barge-type floater, Borisade et al. (2016) and Beyer et al. (2015) conducted the design study using coupled MBS-CFD environment in regular waves and compared with experiments. However, in these studies, the mooring line is modeled as the adjusted global linear stiffness aiming at the preliminary design, though the dynamic response prediction of barge-type floaters is significantly affected by the mooring line model. In the reviews by Davidson and Ringwood (2017) and Aliyar (2022), mooring line models is categorized into three typical types: static, quasi-static, and dynamic mooring line models. Static models, such as linear stiffness matrices and spring models, are commonly used for preliminary designs. Quasi-static models have been employed to design mooring systems, which neglect dynamic effects such as inertia and drag forces. Quasi-static models may be sufficient when displacements are relatively small (Thomsen et al., 2017), but they lead to underestimations of line tension under extreme conditions. To fully account for the dynamic characteristics of mooring lines, dynamic mooring line models based on Newton's second law have been developed, including first-order lumped mass model MoorDyn (Hall and Goupee, 2015) and higher-order finite element model MooDy (Palm et al., 2017). Some studies have coupled dynamic mooring line model with numerical water tanks for some platform types including buoys (Palm et al., 2016; Lee et al., 2021; Jiang et al., 2021; Chen and Hall, 2022), TLP types (Nematbakhsh et al., 2015), semi-submersible types (Martin and Bihs, 2021; Eskilsson and Palm, 2022), and spar types (Aliyar et al., 2022). It is also necessary for barge-type floaters to validate the prediction accuracy of floater motion using numerical water tanks coupled with dynamic mooring line models.

In engineering model, hydrodynamic models are essential to predict floater response accurately. Hydrodynamic loads include contributions from added mass, radiation damping, buoyancy, linear wave excitation forces, nonlinear drag forces and wave drift forces. Linear wave excitation force is conventionally evaluated by potential theory in engineering model. Wang et al. (2021) validated the wave excitation forces in bichromatic waves predicted by numerical water tank for semi-submersible floaters. The errors and uncertainties of the experimental results and CFD simulations were comprehensively described. The uncertainties of measured wave amplitudes from the positioning of the wave probes, and the correction methods for the normalization of wave excitation force were proposed by removing the contributions from the reflected waves from the wave basin and the difference-frequency waves on the wave excitation forces. However, the validation of wave excitation forces and its normalized forces had not been performed for the barge-type floaters. It is found that the normalized wave excitation forces using the measured wave height in the small wave case overestimates those predicted by the potential theory in a wave excitation water tank test for the barge-type floater conducted in this study. The reason of its overestimation needs to be investigated using numerical water tank.

The nonlinear drag force models considering Reynolds numbers and KC numbers were proposed based on the experiment and numerical models (Ishihara and Liu, 2020). Otori et al. (2023) proposed the nonlinear drag force models for barge-type floater considering Reynolds number and KC number based on the nonlinear drag force predicted by numerical forced oscillation simulations with the oscillation period from 0.8 s to 2.0 s in 1/100 model scale. The wave periods were set based on the range possible in a forced oscillation experiment in 1/100 model scale at that time. However, in free decay simulation by engineering model with the proposed nonlinear drag force model, the predicted floater displacements showed the underestimation of damping ratio in the surge direction. The nonlinear drag force on a longer oscillation period of 3.5 s corresponding to surge natural period in 1/100 model scale needs to be investigated by using numerical water tank, which is not able to be investigated in water tank tests.

The wave drift Quadratic Transfer Function (QTF) is important for accurately predicting the mean displacement of the floater. To evaluate the wave drift QTF, experiments are often conducted by restraining a platform model with a soft spring system, which includes springs and pulleys (Ikoma et al., 2021; Seo et al., 2021). Because such experiments are expensive to perform, the wave drift QTF predicted by Newman's approximation (Newman, 1974) based on potential theory is generally used. However, in regular wave simulation by engineering model, the predicted mean displacements in the surge direction underestimated the measurements for most wave periods and overestimated the measurements at the heave natural period of 1.0 s in 1/100 model scale for barge-type floater (Otori et al., 2023). This may be related with the fact that the wave drift QTF predicted by the Newman's approximation underestimated the measured QTF at water tank test (NEDO, 2018). Molin and Lacaze (2016) analytically demonstrated that potential theory overestimates the wave drift QTF prediction at the heave natural period because it does not account for viscous damping in the heave motion. The applicability of numerical water tank on the prediction of wave drift QTF needs to be investigated, because the numerical water tank can take into account viscous effects.

In conventional drag force models, a global matrix of drag coefficients is evaluated from the horizontal and vertical drag coefficients distributed over Morison elements. However, the predicted dynamic response in the regular wave analysis underestimated the measurements for wave periods shorter than the pitch natural period in the surge direction (Otori et al., 2023). Ishihara and Zhang (2019) pointed out that distributed horizontal and vertical drag coefficients in the member-level Morison elements of a semi-submersible floater resulted in underestimation of surge-pitch coupling terms compared to measurements. The impact of underestimating surge-pitch coupling term on the floater motion was limited for semi-submersible floaters, but could lead to an underestimation of the surge response for barge-type floaters. The surge-pitch coupling terms of the drag force needs to be evaluated by forced oscillation simulation using numerical water tank and it is necessary to propose a correction method for the conventional drag force model.

This study investigates the applicability of numerical water tank for the dynamic analysis of barge-type floating platform. The hydrodynamic models in engineering models are improved using numerical water tank. In Section 2, the numerical water tank is set up coupling dynamic mooring line model with the floater motion. The prediction accuracy of numerical water tank is validated with experimental results for wave excitation forces, free decay responses, and dynamic responses in regular waves. In Section 3, the application of the numerical water tank on hydrodynamic force prediction for engineering model is presented. Normalized wave excitation force, horizontal drag coefficient, wave drift QTF, and surge-pitch coupling terms of drag force are predicted by using the numerical water tank. Finally, conclusions are presented in Section 4.

2. Numerical models

In this section, the numerical water tank is developed to conduct the wave excitation simulation and the dynamic response simulation for a barge-type floater. The governing equations are described in Section 2.1. The configuration of computational domain is described in Section 2.2. The boundary conditions are described in Section 2.3. The dynamic mooring line model is described in Section 2.4. Using the developed numerical water tank, the wave excitation force and dynamic response of floating platform are predicted and validated by comparing them with experimental results in Section 2.5.

2.1. Governing equations

A fully nonlinear Navier-Stokes numerical dynamic response simulation of floater in waves is conducted within the open-source CFD toolbox OpenFOAM® (Weller et al., 1998) version 1812+, extended with the waves2Foam package (Jacobsen et al., 2012). We employ the two-phase incompressible Navier-Stokes equations in combination with the Volume of Fluid (VOF) surface capturing scheme developed by Hirt and Nichols (1981). The governing equations used in the Navier-Stokes/VOF solver for the conservation of mass and momentum in an incompressible flow of air and water are specified by Eqs. (1) and (2).

$$\nabla \bullet \boldsymbol{u} = 0 \tag{1}$$

$$\frac{\partial \rho \boldsymbol{u}}{\partial t} + \nabla \bullet \left(\rho \boldsymbol{u}\boldsymbol{u}^T\right) = -\nabla p^* - (\boldsymbol{g} \bullet \boldsymbol{x})\nabla\rho + \nabla \bullet \mu\left(\nabla \boldsymbol{u} + (\nabla \boldsymbol{u})^T\right) + f_\sigma \tag{2}$$

where $\nabla = (\partial_x, \partial_y, \partial_z)$ is the three-dimensional gradient operator, $\boldsymbol{u} = (u_1, u_2, u_3)$ is the velocity field in Cartesian coordinates, $\boldsymbol{g}$ is the gravitational acceleration, $\boldsymbol{x} = (x, y, z)$ is the Cartesian coordinate vector, and f_σ is the surface tension. p^* is the hydrodynamic pressure, which relates to the total pressure, p, by the following equation.

$$p^* = p - \rho(\boldsymbol{g} \bullet \boldsymbol{x}) \tag{3}$$

The local density, ρ, and the local viscosity, μ, are defined in terms of the water volume fraction, α, formulated as Eqs. (4) and (5):

$$\rho = \alpha\rho_{water} + (1-\alpha)\rho_{air} \tag{4}$$

$$\mu = \alpha\mu_{water} + (1-\alpha)\mu_{air} \tag{5}$$

where α is zero for air, one for water and a mixture of the two for all intermediate values. After obtaining the velocity field by solving Eqs. (1) and (2) for the two-phase flow of air and water, the field of α is advanced in time by following the transportation equation of Eq. (6) formulated by Rusche (2003) as:

$$\frac{\partial \alpha}{\partial t} + \nabla \bullet (\boldsymbol{u}\alpha) + \nabla \bullet (\boldsymbol{u}_r \alpha(1-\alpha)) = 0 \tag{6}$$

Solving the original transportation equation of the VOF method would lead to significant smearing of the interface. As discussed in Berberović et al. (2009), Eq. (6) significantly reduces the smearing by introducing an artificial compression term, which is the last term of the left-hand side. The artificial compression term is only active in the vicinity of the interface, i.e., $0 < \alpha < 1$, where its strength is governed by the relative velocity, $\boldsymbol{u_r}$. To ensure the boundedness of α between 0 and 1 in solving the transportation equation of Eq. (6), a multi-dimensional flux limited scheme (MULES) is used.

OpenFOAM® is based on finite volume (FV) discretization, which applies conservation principles to a finite region in space known as control volume. Table 1 summarizes the numerical schemes used in this study for each term in the governing equation Eqs. (1), (2) and (6).

Table 1
Numerical schemes used in this study.

Term		Discretization
Time scheme		Euler, First-order implicit
Gradient scheme		Second-order central difference
Divergence	$\nabla \bullet (\rho \boldsymbol{u})\boldsymbol{u}^T$	First-order upwind
	$\nabla \bullet \mu\left(\nabla \boldsymbol{u} + (\nabla \boldsymbol{u})^T\right)$	Second-order central difference
	$\nabla \bullet \boldsymbol{u}\alpha$	MUSCL, Second order TVD
	$\nabla \bullet \boldsymbol{u}_r\alpha(1-\alpha)$	Second-order central difference

The six degrees of freedom motion for the floating platform is solved using the rigid body dynamics solver in OpenFOAM, *rigidBodyMotion*. The equations of motion are formulated based on the conservation of linear and angular momentum:

$$\frac{\partial \boldsymbol{v_f}}{\partial t} = \frac{\boldsymbol{F_f}}{m_f} \tag{7}$$

$$\frac{\partial \boldsymbol{\omega_f}}{\partial t} = \boldsymbol{I_f}^{-1} \bullet \left(\boldsymbol{M_f} - \boldsymbol{\omega_f} \times \left(\boldsymbol{I_f} \bullet \boldsymbol{\omega_f}\right)\right) \tag{8}$$

where $\boldsymbol{v_f}$ and $\boldsymbol{\omega_f}$ are the linear and angular velocity of the floater, respectively. m_f denotes the mass of the floater, and $\boldsymbol{I_f}$ denotes the tensor of inertia of the floater. $\boldsymbol{F_f}$ and $\boldsymbol{M_f}$ represent total external forces and moments acting on the floater, including fluid forces, mooring line forces, and the gravitational force, and are given by:

$$\boldsymbol{F_f} = \iint_{S_{cell}} (p\boldsymbol{n} + \boldsymbol{\tau}) \bullet d\boldsymbol{S_{cell}} + \boldsymbol{F_M} + \boldsymbol{F_g} \tag{9}$$

$$\boldsymbol{M_f} = \iint_{S_{cell}} \boldsymbol{r_{CS}} \times (p\boldsymbol{n} + \boldsymbol{\tau}) \bullet d\boldsymbol{S_{cell}} + \boldsymbol{r_{CM}} \times \boldsymbol{F_M} + \boldsymbol{r_{CG}} \times \boldsymbol{F_g} \tag{10}$$

In these expressions, the fluid forces are computed by integrating the normal pressure, p and tangential shear stress, $\boldsymbol{\tau}$ across all patches enclosing the body. $\boldsymbol{F_M}$ is the mooring line tensions calculated using dynamic mooring line model described later in Section 2.4. $\boldsymbol{F_g}$ is the gravitational force. $\boldsymbol{r_{CS}}$, $\boldsymbol{r_{CM}}$ and $\boldsymbol{r_{CG}}$ denote the distance vector of the structural mass center to the cell surface center, the fairlead of mooring line, and the center of gravity, respectively.

The coupling of floating body motion with free surface flow is achieved in a segregated manner with a PIMPLE loop, which is a combination of SIMPLE and PISO algorithms. Based on the linear and angular accelerations evaluated from Eqs. (7) and (8), the displacement and velocity of the floater is updated with the Newmark method at every time step.

2.2. Computational domains

The dimension of computational domain follows the water tank size in the experiment. The entire computational domains for the wave excitation and dynamic response simulations are shown in Fig. 1(a) and (b), respectively. The domain for the wave excitation simulations is set at the model scale of 1:100 to be consistent with the water tank experiment conducted in Section 3.1.1 for validation purposes. The domain for the dynamic response simulations is also set up at the model scale of 1:100 to be consistent with the water tank experiment conducted by Otori et al. (2023). A structured mesh is used for the discretization of the whole computational domain. The grid size is 0.015 m with the expanding factor from 1.0 to 1.06. To resolve the flow separation and deformation of the free surface caused by the platform motion, the castellated mesh refinement is applied in the region near the platform as shown in Fig. 2, following the study in Otori et al. (2023).

The configuration of the floating platform model and the definition of coordinates are depicted in Fig. 3. The main body of the floater is

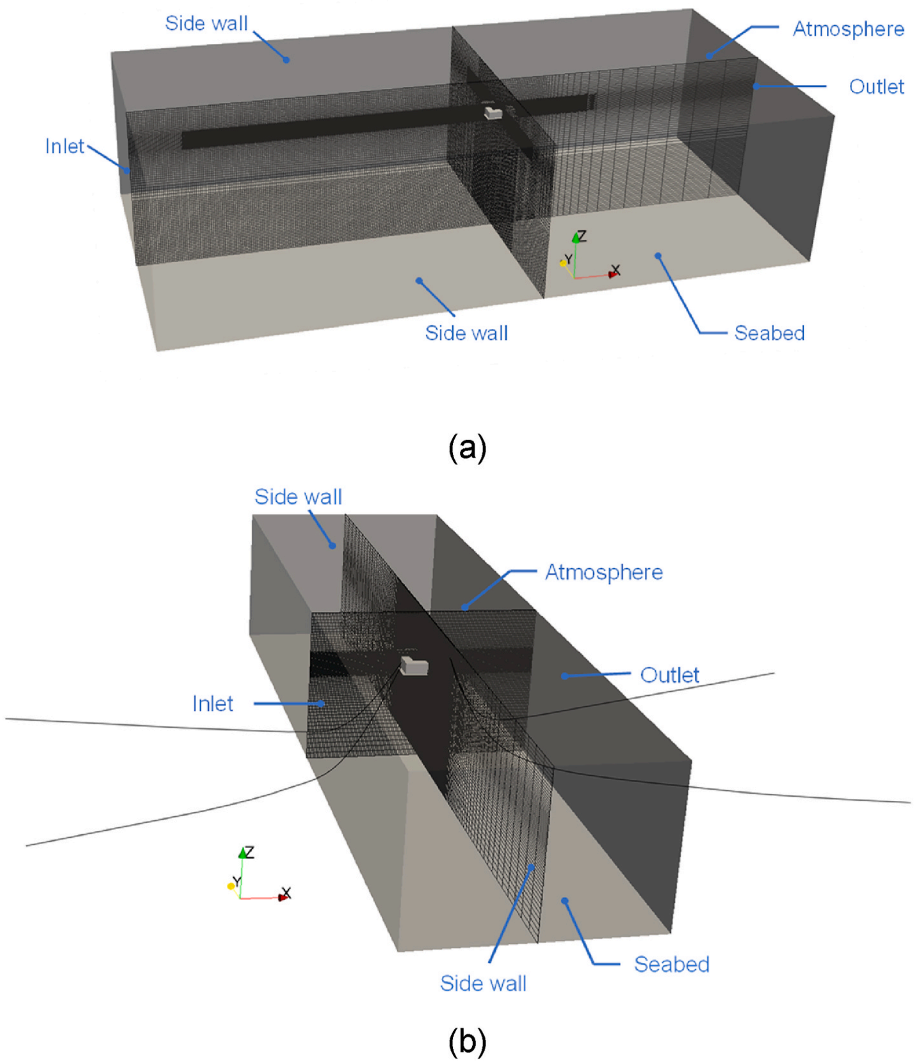

Fig. 1. Overview of the computational domain of numerical water tank. (a) Wave excitation simulation. (b) Dynamic response simulation.

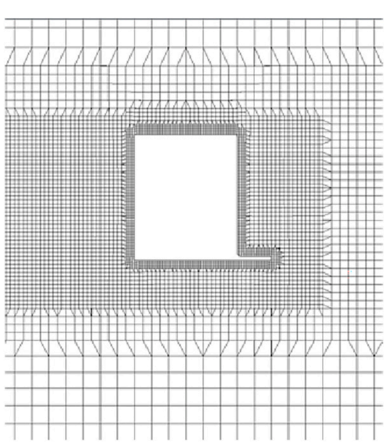

Fig. 2. The Z-X plane view of the computational grid around the model.

rectangular with a width of 0.45m in the X and Y directions and a draft of 0.07 m. A moonpool with a width of 0.27 m is placed in the center of the floater. Skirts with a width of 0.03 m and a thickness of 0.0035 m are attached to the bottom of the floater. The coordinate origin is located at the center of the floater (in the X and Y directions) and at the free surface (in the Z direction), with X in the surge direction, Y in the sway direction, and Z in the heave direction. The measured center of gravity, COG, is located at (0.00579, 0, 0.055) m. The measured radii of gyration are 0.208 m in the roll direction and 0.209 m in the pitch direction. Table 2 shows the main properties of the floater.

2.3. Boundary conditions

Boundary conditions are set up as shown in Table 3 for the computational domains depicted in Fig. 1. At the atmosphere boundary of α, the Neumann condition is applied when the fluids flow out of the domain, while the Dirichlet condition is applied when the fluid flows into the domain. At the seabed and side walls, the slip condition is imposed. A no-slip condition is applied to the floater.

The inlet and outlet boundaries employ the wave generating/absorbing boundary conditions (GABC) developed by Borsboom and Jacobsen (2021). Reddy and Viré (2022) indicated that the GABC method offers advantages in reducing spatial and temporal wave height decay and eliminating computational costs related to the relaxation zone. The inlet and outlet boundaries absorb the waves outgoing from the computational domain. The GABC method applies the state-of-the-art Sommerfeld-type radiation condition at the open boundaries. The original Sommerfeld condition for absorbing boundary condition (ABC) is expressed as Eq. (11):

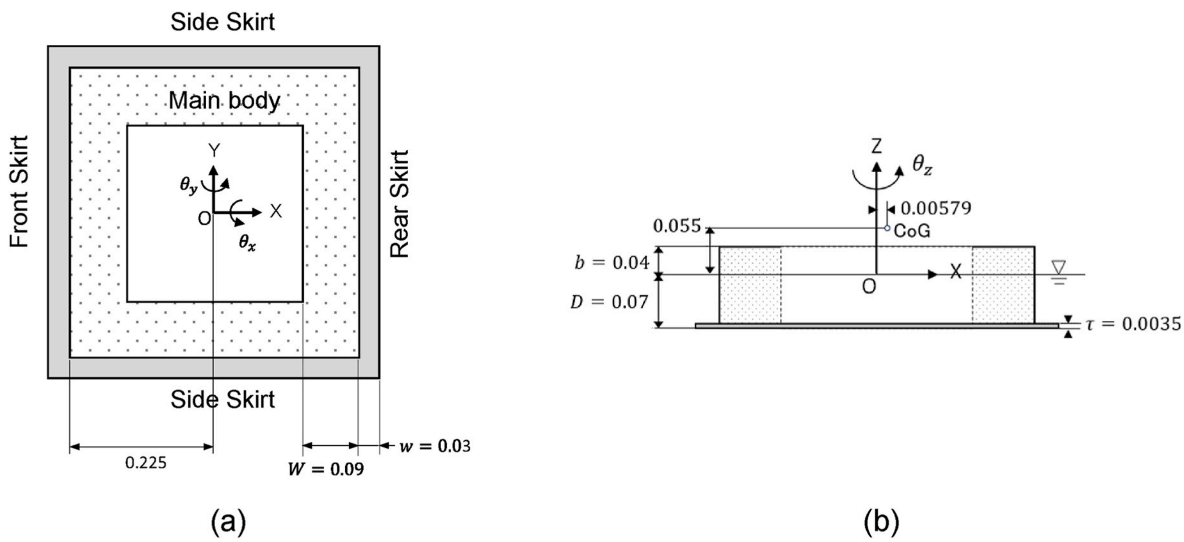

Fig. 3. Configuration of the 1:100 scale floater and the definition of coordinates (unit: m). (a) Top view of X-Y plane. (b) Side view of Z-X plane.

Table 2
Dimensions and hydrostatic properties of the 1:100 scale floater.

Element	Symbol	Dimension
Draft [m]	D	0.07
Freeboard (Elevation of the tower base) [m]	b	0.04
Width of the beam of main body [m]	W	0.09
Width of the skirt extended from the main body [m]	w	0.03
Thickness of skirt [m]	τ	0.0035
Area of skirt in X-Y plane [m^2]	S	0.0576
Center of gravity (X, Y, Z) [m]	COG	(0.00579, 0, 0.055)
Radius of gyration in the roll direction [m]	k_{XX}	0.208
Radius of gyration in the pitch direction [m]	k_{YY}	0.209

$$\frac{\partial\phi}{\partial t} + c\frac{\partial\phi}{\partial x} = 0, x = 0, -h \le z \le 0 \tag{11}$$

where $c = \omega/k$ gives the speed of wave propagation. ω is a cyclic frequency and k is the wave number of the propagating waves. h is the water depth. For simplicity, the right boundary is placed at $x = 0$. ϕ is the two-dimensional velocity potential. The Sommerfeld condition of Eq. (11) perfectly absorb waves at a single frequency, ω by tuning the value of c. However, it does not perfectly absorb waves with different frequencies, because they propagate at different speeds. To solve this problem, Borsboom and Jacobsen (2021) proposed to use a depth-varying coefficient $c(z) = \sqrt{gh}a(z)$ instead of a constant value in the Sommerfeld-type condition:

$$\frac{\partial\phi}{\partial t} + c(z)\frac{\partial\phi}{\partial x} = 0, x = 0, -h \le z \le 0 \tag{12}$$

where $a(z)$ is determined by minimizing the reflection coefficient.

The inlet boundary also generates the incoming waves according to the specified wave period, wave height, and water depth. For GABC, wave generation condition is added to the ABC of Eq. (12). The governing equation is formulated as Eq. (13):

$$\frac{\partial\phi}{\partial t} + c(z)\frac{\partial\phi}{\partial x} = \frac{\partial\phi_{giv}}{\partial t} + c(z)\frac{\partial\phi_{giv}}{\partial x}, x = 0, -h \le z \le 0 \tag{13}$$

where ϕ_{giv} is the velocity potential for the prescribed incident wave.

2.4. Modeling of mooring lines

The finite element model Moody developed by Palm et al. (2017) is coupled with the body motion solver in OpenFOAM to predict accurately the floater motion in the pitch direction in waves. It uses an *hp*-adaptive discontinuous Galerkin method with the intent of predicting snap loads. The high-order formulation makes engineering accuracy achievable using only a few high order elements. External forces acting on the cables include the added mass and Froude-Krylov forces, the drag force, the net force of gravity and buoyancy, and seabed contact forces. The bending stiffness of the mooring line is neglected. The summed restraint forces and moments are returned to solve the motion of the floater described in Section 2.1. Readers are referred to the original references for detailed descriptions of the model (Palm et al., 2017).

Numerical settings related to the mooring line model are listed in Table 4. The number of spatial discretization of each mooring line is chosen as 100. Reducing the number to 20 results changes the predicted tension by less than 0.2 % in the static condition, but causes high-frequency noise at the beginning of the calculation. This noise is not observed when the number of elements is larger than 100. The equation of motion of the mooring line is advanced in time with the third order

Table 3
Description of the boundary conditions for volume fraction, hydrodynamic pressure and velocity.

Items	α	p*	*u*
Atmosphere	Neumann condition: $\partial\alpha/\partial n = 0$ when the fluid flows out of domain. Dirichlet condition: $\alpha = 0$ when the fluid is flowing into the domain	Dirichlet condition: $p^* = 0$	Neumann condition: $\partial u/\partial n = 0$, Except for the tangential component which is set to 0 for inflow.
Seabed	Slip	Slip	Slip
Side walls	Slip	Slip	Slip
Inlet and outlet	Neumann condition: $\partial\alpha/\partial n = 0$	Wave generating/absorbing boundary conditions	Wave generating/absorbing boundary conditions
Structure of floater	Neumann condition: $\partial\alpha/\partial n = 0$	Neumann condition: $\partial p^*/\partial n = 0$	No-slip wall

Table 4
Numerical settings related to the mooring line model.

Items	Modeling
Mooring line model	Dynamic mooring line model MooDy (Palm et al., 2017)
Number of FEM elements per one mooring line	100
Time stepping schemes in MooDy	Third-order explicit Runge-Kutta scheme
Time step size in MooDy	Adaptive time step with maximum CFL number of 0.9
Time stepping schemes in CFD solver	Euler implicit
Time step size in CFD solver	Fixed time step

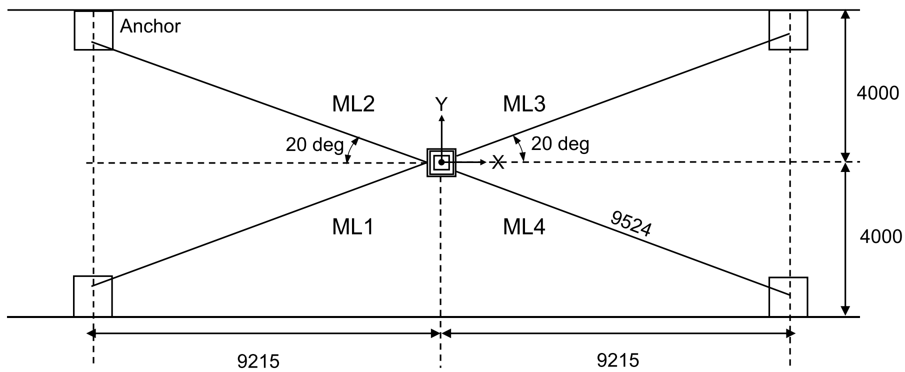

Fig. 4. Top view of the mooring system in the dynamic response experiment (unit: mm).

Table 5
The initial displacement of the floater and the mooring line tension in the static equilibrium test.

Item	Measurement	Prediction	Error
Surge	−0.0026 m	−0.0026 m	0 %
Heave	0 m	0 m	0 %
Pitch	1.1 deg	1.1 deg	0 %
Mooring line tension in ML1	3.78 N	3.76 N	−0.5 %
Mooring line tension in ML3	3.72 N	3.74 N	+0.5 %

explicit Runge Kutta scheme, with adaptive time step size determined by a maximum Courant Friedrichs Lewy (CFL) number of 0.9. The time stepping scheme and time step size of the CFD solver significantly influence the stability in coupling with MooDy. The Euler implicit method is used for the time stepping scheme. Using the Crank-Nicolson method results in high-frequency noise of the mooring line tension that diverges over time as observed in Lee et al. (2021), even though the Crank-Nicolson method provides higher-order accuracy compared to the Euler implicit method. For the time step size, a fixed time step is used, because adaptive time step for time step size results in high-frequency noise in the mooring line tension, as reported in the study by Palm et al. (2016). This numerical high-frequency noise occurs because the Moody is modeled without the bending stiffness (Palm et al., 2016), and causes an ill-posed problem (Triantafyllou and Howell, 1994) associated with the negative prediction of tension near the touch-down point of mooring line.

Based on the dynamic response water tank test described in Otori et al. (2023), four mooring lines, i.e., ML1 to ML4, are attached to the platform as shown in Fig. 4. The angles of mooring lines are 20° to the X-axis, and the fairleads are located at $X = -0.265\ m$, $Y = \pm 0.0\ m$ and $Z = 0.04\ m$ for ML1 and ML2 and at $X = 0.265\ m$, $Y = \pm 0.18\ m$ and $Z = 0.04\ m$ for ML3 and ML4. The length of each mooring line is 9.86 m. The studless chains are modeled as cylindrical elements with a diameter of 4.9 mm, and the weight of 1.43 N/m in air and 1.25 N/m in water. The added mass coefficient and drag coefficient of lines are set to the same as in Otori et al. (2023).

The measured and predicted initial displacement of the floater and the mooring line tension are summarized in Table 5 for the static equilibrium test. Due to the cable for measuring the mooring line tension, the initial displacement of 1.1 deg in the pitch direction is observed in the experiment. Instead of modeling the cable, the coordination of the center of gravity of the floater is shifted to 5.8 mm in the X-direction to reproduce the initial displacement. The length of ML1 and ML2 is shortened by 2.9 mm (0.03 % of the total length) and that of ML3 and ML4 is by 2.1 mm (0.02 % of the total length) to reproduce the measured mooring line tension.

2.5. Validation of numerical water tank

2.5.1. Validation of the predicted wave excitation forces

To validate the numerical simulation, wave loads are measured at the small towing tank of Akishima Laboratory (Akishima Laboratory, 2024) in this study. The configuration of the water tank is illustrated in Fig. 5. The dimensions of the water tank are 100 m in length, 5.0 m in width, and 2.65 m in depth, with a set water depth of 2.15 m. A 3-component force transducer, fixed to a 1:100 scale barge-type platform model, measures the wave excitation forces and moments in the surge, heave, and pitch directions. The incoming wave is measured at the wave probe located upstream of the platform at $X = -4.51\ m$ and $Y = 0.0\ m$. The incoming wave period T_w is set at a typical value of 1.2 s. Two different wave height conditions are set at $H = 0.02\ m$ and $H = 0.04\ m$.

Numerical simulations are performed to predict the wave load on a fixed barge-type platform. The computational domain for wave excitation simulation described in Fig. 1 (a) is employed. The dimension of the computational domain is illustrated in Fig. 6. The incoming waves are generated at the GABC inlet and propagate in the positive X-direction. The length between the outlet boundary and the platform model, length b in Fig. 6, is set as 4.5 m, corresponding to two wavelengths. The length from the platform model to the inlet boundary, length a in Fig. 6, is set to 6.0 m, which is longer than b, so that the computational domain includes the wave probe position. The air phase depth c, the water phase depth d, and the length of the computational domain in the Y-direction (i.e., the

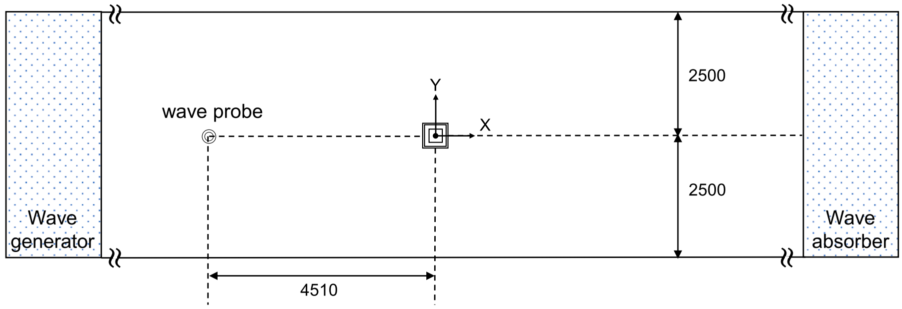

Fig. 5. Top view of the wave excitation experiment (unit: mm).

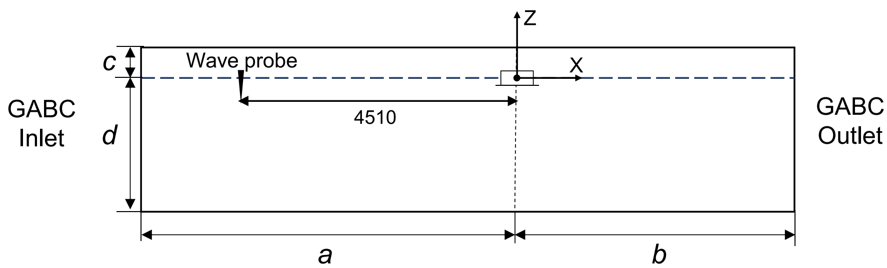

Fig. 6. Layout of computational domain for the wave excitation simulation (unit: mm).

Table 6
Predicted wave height at the wave probe (X = -4.51m) in the experiment and simulation.

Cases	Exp.	CFD	Error
$H = 0.02\,m$	0.0156m	0.0144 m	−7.8 %
$H = 0.04\,m$	0.0314m	0.0300 m	−4.4 %

distance between side walls in Fig. 1 (a)) are set as 0.5 m, 2.15 m and 5 m respectively as same as the water tank experiment layout. The incoming wave is evaluated at $X = -4.51\ m$ and $Y = 0.0\ m$, which corresponds to the position of the wave probe in the experiment.

The incoming wave height at the wave probe, H_{Probe}, and phase, ε_{Probe}, are evaluated by assuming that the surface elevation at the wave probe η_{Probe} represents a sinusoidal wave as in Eq. (14):

$$\eta_{Probe} = \frac{H_{Probe}}{2}\sin(\omega t - kX_{Probe} - \varepsilon_{Probe}) \tag{14}$$

where ω denotes the wave frequency, and k is the wave number. X_{Probe} is the position of the wave probe in the X-direction of $-4.51m$. The predicted incoming wave height at the wave probe, H_{Probe} is compared with the experimental values in Table 6. It is confirmed that the incoming waves generated in the simulation are approximately the same height as the experiment, with an error within 7.8%.

The predicted wave loads at $H = 0.02$ m and $T_w = 1.2$ sec are compared with the measurements in Fig. 7. The predicted wave loads

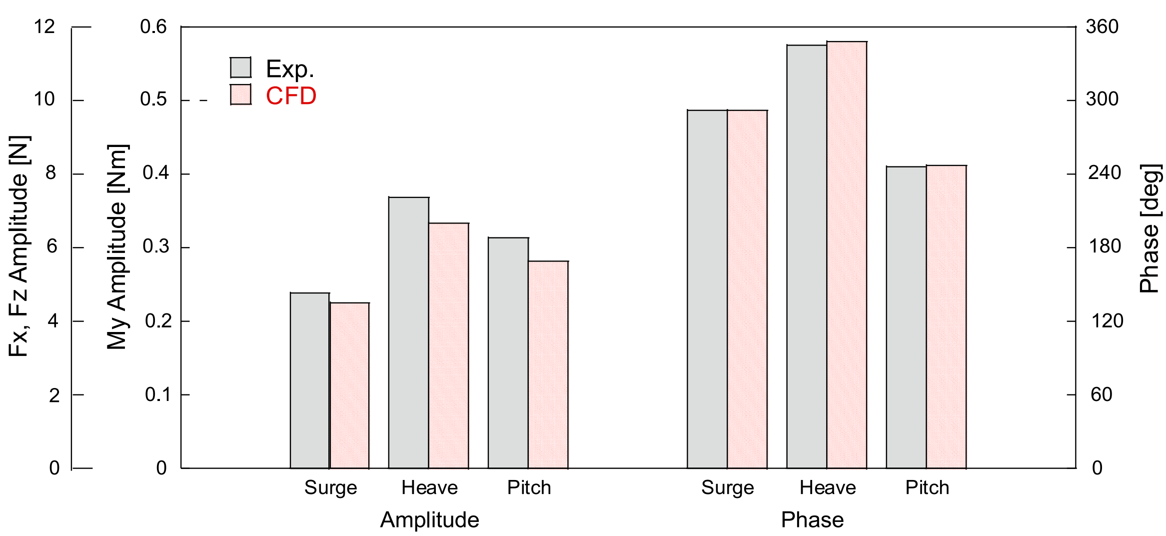

Fig. 7. Measured and predicted wave excitation forces (H = 0.02 m, T_w = 1.2 s).

Table 7
Measured and predicted wave excitation forces ($H = 0.02$ m, 0.04 m, $T_w = 1.2$ s).

	Amplitude [N, Nm]				Phase [deg]			
	H = 0.02 m		H = 0.04 m		H = 0.02 m		H = 0.04 m	
	Exp.	CFD (Error)	Exp.	CFD (Error)	Exp.	CFD (Error)	Exp.	CFD (Error)
Surge	4.77	4.50 (−5.7%)	9.15	9.13 (−0.2%)	292.0	291.8 (−0.2 deg)	302.0	306.3 (+4.4deg)
Heave	7.38	6.67 (−9.7%)	13.47	13.14 (−2.5%)	344.9	348.2 (+3.3 deg)	342.7	350.1 (+7.4deg)
Pitch	0.313	0.282 (−10.0%)	0.722	0.708 (−2.0%)	246.5	247.2 (+0.7 deg)	234.0	240.6 (+6.4deg)

accurately match the measurements in the surge, heave, and pitch directions, with amplitude errors within 10 % and phase errors within 7.4 deg. The amplitude errors can be mainly attributed to the 7.8% difference in incoming wave height, as shown in Table 6. The measured and predicted wave excitation forces at $H = 0.04\ m$ are also listed in Table 7. It is confirmed that the predicted wave loads are in good agreement with experiment for different wave heights.

2.5.2. Validation of the predicted floater responses in free decay simulation

Free decay simulations are conducted and validated by comparing to the water tank test conducted in Otori et al. (2023). The computational domain for dynamic response simulation described in Fig. 1 (b) is employed. The dimension of computational domain is illustrated in Fig. 8. The length from the floater to the inlet and outlet boundaries, denoted as a and b in Fig. 8, is set to $a = b = 1.1\ m$, which is confirmed to be sufficient to eliminate the influence on the predicted dynamic response during simulations. The air phase depth, c, the water phase depth, d, and the length of the computational domain in the Y-direction (i.e., the distance between side walls in Fig. 1 (b)) are set as 0.5 m, 1.0 m and 8.0 m respectively as same as the water tank test. The initial displacements for the free decay simulations are set according to the water tank tests, which are respectively −0.087 m, −0.029 m, and 5.4 deg in the surge, heave, and pitch directions.

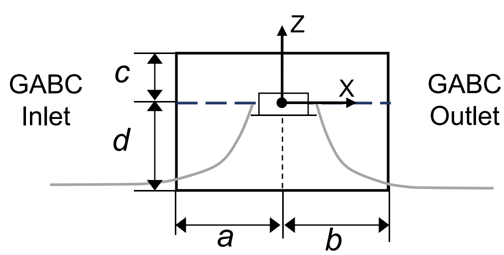

Fig. 8. Layout of computational domain for the dynamic response simulation.

The time series of the predicted floater motion are validated by comparing to the experiment by Otori et al. (2023) in Fig. 9. The time axis is normalized by the natural periods obtained in experiments for each direction: $T_{n1} = 3.50$ s for surge, $T_{n3} = 0.86$ s for heave, and $T_{n5} = 1.21$ s for pitch. The displacement is normalized by the absolute initial displacements in each direction. The predictions by numerical water tank show excellent agreement with the experiment for the surge, heave, and pitch directions. The prediction by numerical water tank also captures well the two-peak phenomena in the heave direction as a composite of two oscillation periods around 0.72 s and 1.0 s, due to the oscillation of water mass in the moonpool. The natural periods and damping ratios are analyzed from the first twelve peaks of oscillation and presented in Fig. 10. For the heave direction, the natural period and

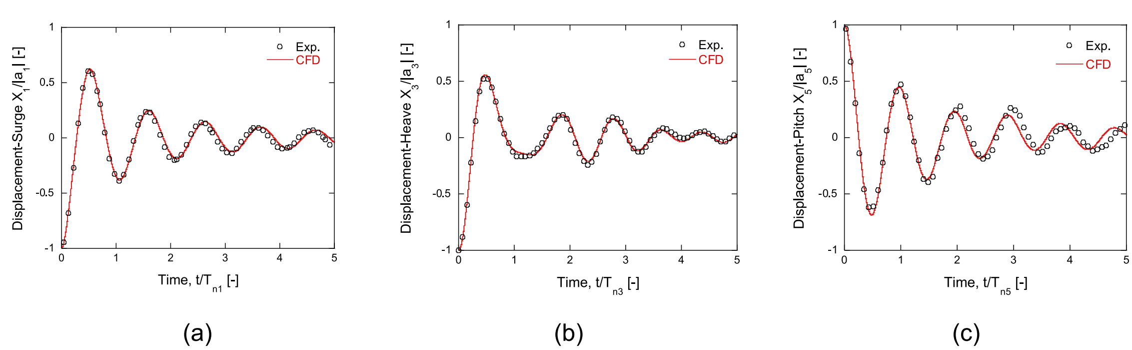

Fig. 9. Measured and predicted time series of floater displacement in free decay in (a) surge, (b) heave, and (c) pitch directions.

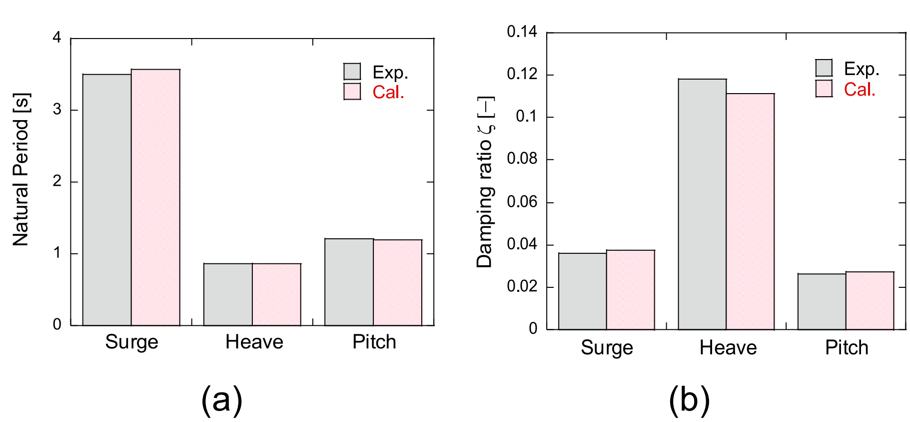

Fig. 10. Measured and predicted (a) natural periods and (b) damping ratios.

damping ratio are calculated from the initial displacement and the first positive peak. The natural periods in the surge, heave, and pitch directions match well with the experiments within 2.0 %. The damping ratios match well with the experiments within 6.0 %. The numerical water tank has demonstrated the accurate prediction of free decay responses.

2.5.3. Validation of the predicted floater responses in regular waves

Regular wave simulations are conducted and validated by comparing to the water tank test results described in Otori et al. (2023). The same layout of computational domain described in Fig. 8 is employed. For incoming wave conditions, eight wave period cases from 0.8 s to 2.0 s are simulated to cover dominant wave periods in real sea states. The designated wave height is set as 0.02 m, which corresponds to the normal sea state. The measured wave heights in the experiments are used as input wave heights for the numerical water tank, which are within a range of −6.1 % to +25 % of the design value.

The predicted mean displacements in the surge, heave, and pitch directions for regular waves are compared with experimental results in Fig. 11. The predictions by the numerical water tank demonstrate a favorable agreement with the experimental results. Notably, the numerical water tank's prediction for surge mean displacement accurately captures the gradual increase observed in shorter wave periods. The predicted amplitude and phase are also compared with the experimental results in Fig. 12. The predictions by the numerical water tank show good agreement with the experimental results. In particular, the prediction by the numerical water tank captures the surge amplitude increasing for periods shorter than 1.3 s and the peak in pitch amplitude at 1.3 s, which is attributed to accurate consideration of drag forces in the surge and pitch directions.

3. Application of numerical water tank for dynamic response analysis

In Section 3, the application of the numerical water tank on hydrodynamic force prediction for engineering model is presented. In Section 3.1, the reason of the overestimation for the normalized wave excitation forces is investigated by wave excitation simulation using numerical water tank. In Section 3.2, the horizontal drag coefficient at a long oscillation period of 3.5 s in a model scale is investigated by forced oscillation simulations using numerical water tank, and the conventional drag coefficient model is extended. In Section 3.3, wave drift force

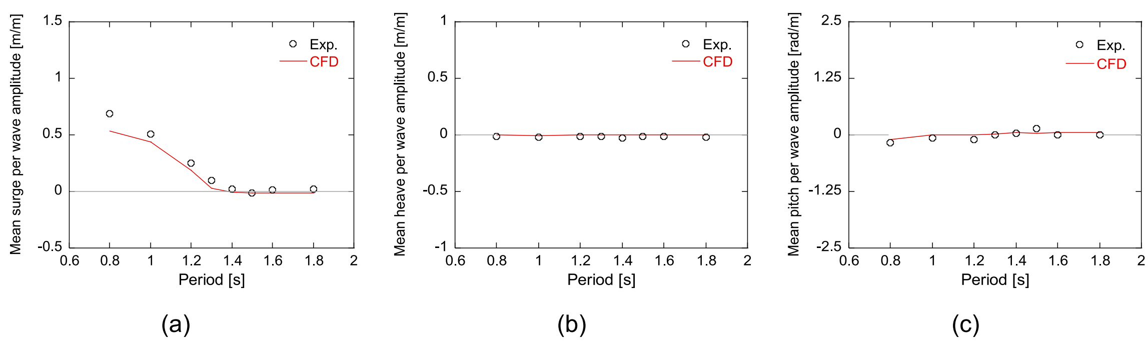

Fig. 11. The measured and predicted of mean floater displacements in regular waves (H = 0.02m) in (a) surge, (b) heave, and (c) pitch directions.

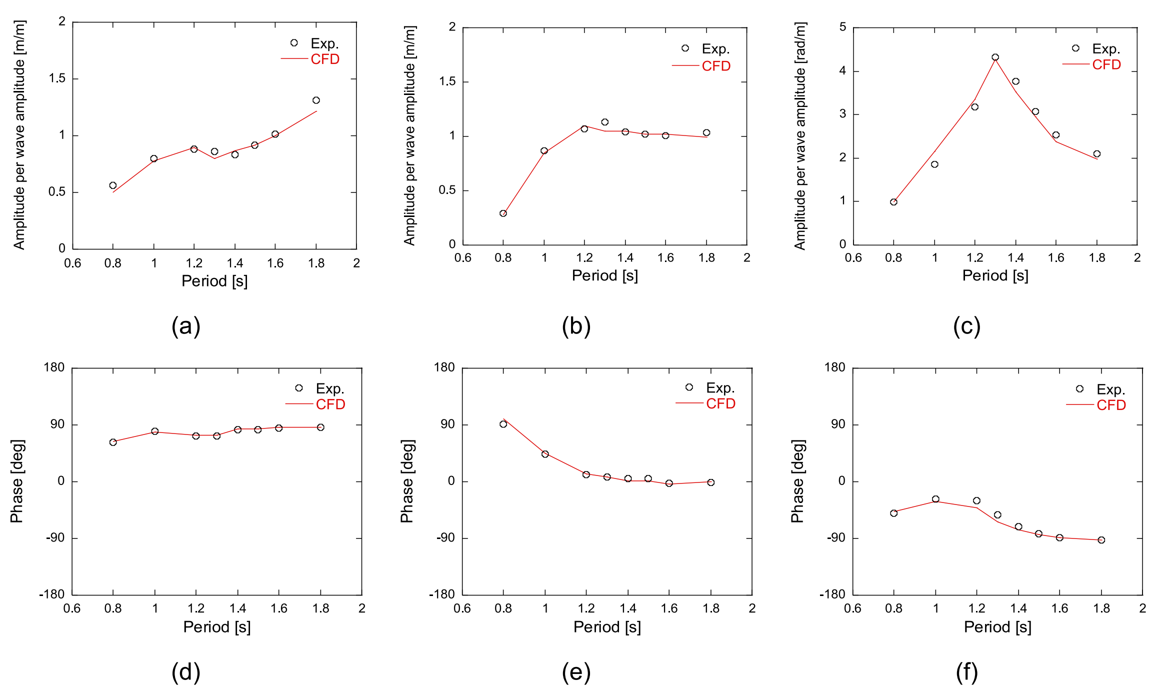

Fig. 12. The measured and predicted amplitude and phase RAO of the floater motions in regular waves (H = 0.02m). Amplitudes in (a) surge, (b) heave, and (c) pitch directions. Phases in (d) surge, (e) heave, and (f) pitch directions.

QTFs are evaluated by regular wave simulation using the numerical water tank to improve the prediction accuracy comparing with Newman's approximation. In Section 3.4, the surge-pitch coupling terms of drag force is investigated by forced oscillation simulation using numerical water tank. A new engineering model analysis procedure is proposed considering the surge-pitch coupling terms of drag force.

3.1. Prediction of the normalized wave excitation forces

In engineering model, normalized linear wave excitation forces need to be considered as one of the hydrodynamic forces. However, the normalized wave excitation forces evaluated for small wave height do not match those predicted by potential theory in the experiment. To investigate its reason, the wave excitation force predicted in Section 2.5.1 for small wave height case ($H = 0.02\,m, T_w = 1.2s$) is normalized by the incoming wave amplitude and compared to the prediction by potential theory calculated by Ansys Aqwa (ANSYS Inc, 2019). The normalized amplitude, $\bar{f}$ and phase, $\overline{\varepsilon_f}$ are calculated as Eqs. (15) and (16), using the amplitude, f and the phase, ε_f of the harmonic component of the predicted wave load, $f\sin(\omega t - \varepsilon_f)$:

$$\bar{f} = \frac{f}{H_{Probe}/2} \tag{15}$$

$$\overline{\varepsilon_f} = \varepsilon_f - \varepsilon_{Probe} \tag{16}$$

Fig. 13 and Table 8 show the predicted normalized wave excitation forces by potential theory and CFD. The predicted normalized amplitudes are larger than those predicted by potential theory by 51.4 % for surge, 41.8 % for heave, and 54.6 % for pitch directions.

The distribution of the free surface elevation is visualized in Fig. 14 by conducting the simulations with and without the floater. In simulations with the floater, it is observed that interference fringes are generated from the interference between the incident wave and its reflected counterpart from the floater, while an undistributed regular wave field is observed in simulations without the floater. Fig. 15 compares the wave height at the probe location during simulations with and

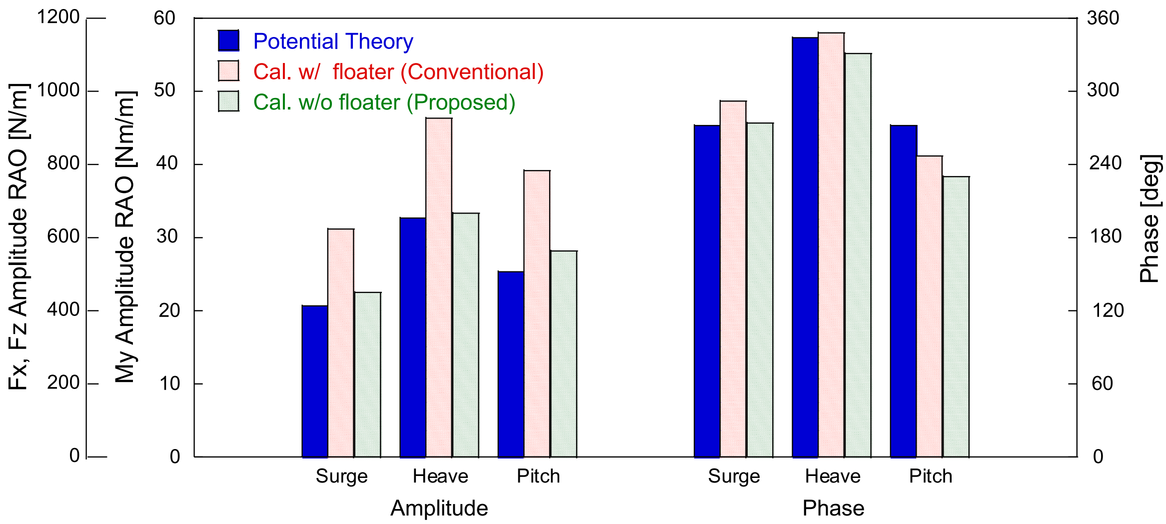

Fig. 13. The predicted normalized wave excitation forces by potential theory and CFD ($H = 0.02\,m, T_w = 1.2\,sec$).

Table 8
Normalized wave excitation forces at $H = 0.02\,m$ and $T_w = 1.2\,s$ predicted by potential theory and CFD for different wave amplitudes.

	Amplitude [N/m, Nm/m]			Phase [deg]		
	Potential theory	CFD, w/floater (Error)	CFD, w/o floater (Error)	Potential theory	CFD, w/floater (Error)	CFD, w/o floater (Error)
Surge	413.0	625.3 (+51.4 %)	449.5 (+8.8 %)	272.0	291.8 (+19.8 deg)	274.4 (+2.4 deg)
Heave	653.0	926.2 (+41.8 %)	665.8 (+2.0 %)	344.4	348.2 (+3.8 deg)	330.8 (−13.6 deg)
Pitch	25.3	39.1 (+54.5 %)	28.1 (+11.1%)	272.0	247.2 (−24.8 deg)	229.8 (−42.2 deg)

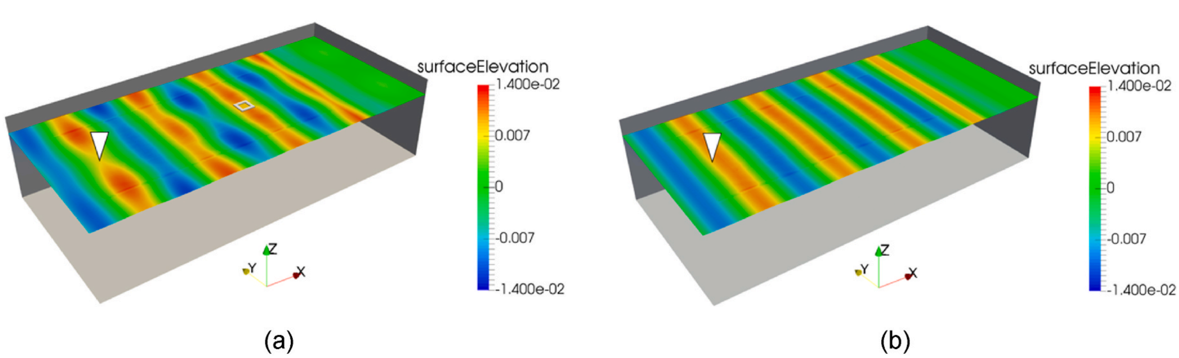

Fig. 14. Visualization of the free surface elevation ($H = 0.02\,m, T_w = 1.2\,sec$). (a) Simulation with the floater. (b) Simulation without the floater.

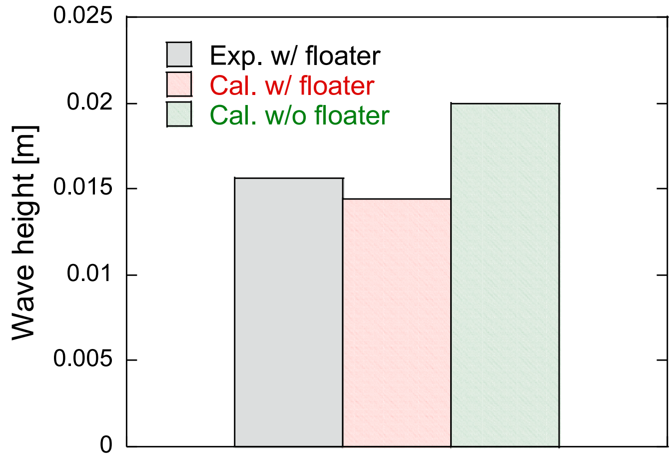

Fig. 15. Wave height at the wave probe measured and predicted in cases with and without the floater.

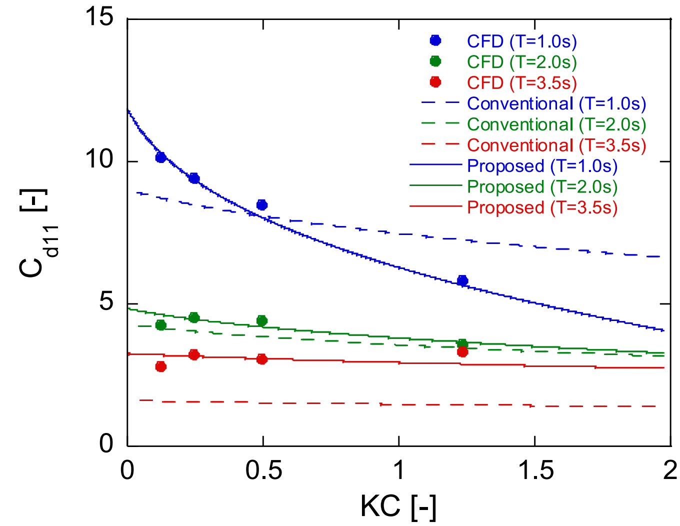

Fig. 16. Horizontal drag coefficients predicted by the numerical simulation, the conventional model and the proposed model.

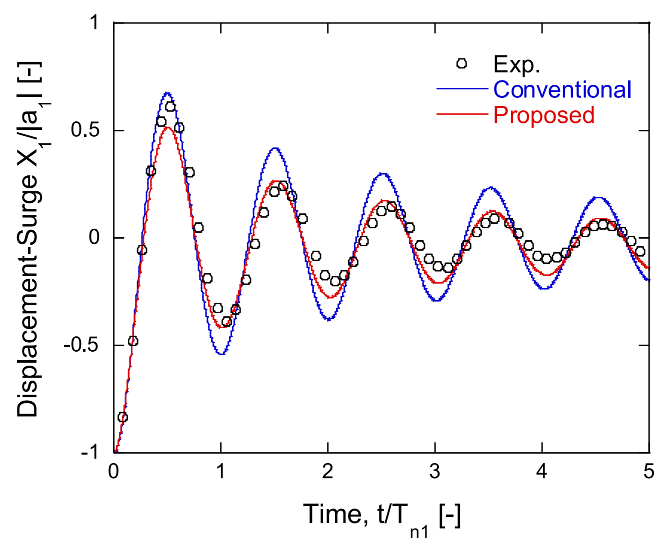

Fig. 17. The time series of surge free decay response measured and predicted using conventional and proposed horizontal drag coefficient models.

without the floater. The wave height from simulations with the floater is found to be smaller by 28% for $H = 0.02\,m$ compared to those without the floater because the wave probe is located at the trough in the interference fringe as marked with pin in Fig. 14. It is clarified that the wave probe location causes the overestimation of the normalized wave excitation force in the experiment.

This indicates that the incoming wave needs to be simulated without the floater. The wave excitation force is normalized by the incoming wave without floater as shown in Fig. 13. The prediction error, $\bar{f}$ of CFD from potential theory for $H = 0.02\,m$ improves significantly from 51.4 % to 8.8 % for surge, from 41.8% to 1.9 % for heave, and from 54.6 % to 11.1 % for pitch, compared to the conventional method normalized by the input wave simulated with the floater. The remaining error comes from the drag force effect since the potential theory assumes the infinitesimal wave height.

3.2. *Prediction of the horizontal drag coefficient*

In engineering model, the drag coefficient needs to be considered in Morison equations. Otori et al. (2023) proposed the horizontal drag coefficient model for the barge-type floater using the predictions by forced-oscillation simulations in the range of wave period from 0.5 s to 2.0 s in 1/100 model scale, which was covered in water tank test. However, with the proposed drag coefficient model, an underestimation of the damping ratio in the surge free decay response has been reported as shown in Fig. 17. In this study, numerical forced oscillation simulations in the surge direction are newly performed at the surge natural period of 3.5 s, which is not able to be performed by the water tank test. Four different amplitudes of 0.005 m, 0.01 m, 0.02 m, and 0.05 m are conducted applying the numerical setups used in Otori et al. (2023). The predicted drag coefficients with different KC numbers are plotted for various oscillation periods in Fig. 16. As the oscillation period increases to the surge natural period of 3.5 s, the KC dependency becomes weaker, and the drag coefficient is almost constant for different KC number. Dashed line in Fig. 16 shows the conventional drag coefficient model. It is found that the conventional model of Otori et al. (2023) underestimates the horizontal drag coefficient at 3.5 s predicted by CFD as shown by dashed line in Fig. 16.

Based on the numerically predicted drag coefficient, the conventional model is extended by introducing the non-dimensional parameters, ξ_1 and γ_1 as functions of the oscillation period, T, as shown in Eq. (17):

$$
\begin{aligned}
C_{d11} &= C_{d11,ref}\left\{-0.45(\gamma_1 KC_1+1)^{0.33}+1.93\right\}\xi_1 \\
\gamma_1 &= 3.8\times10^{-9}\beta^2 \\
\xi_1 &= 1.4\times10^{-9}\beta^2+1.6 \\
KC_1 &= \frac{2\pi a_1}{R},\ \beta=\frac{R^2}{\nu T}
\end{aligned}
\tag{17}
$$

where $C_{d11,ref}$ is the reference drag coefficient with an amplitude of 0.02 m and an oscillation period of 3.5 s (i.e., the natural period in the surge direction). KC_1 is the KC number in the surge direction. β is the normalized frequency. $R = 0.255\,m$ is the representative length of floater, employing the half length of skirt. ν is the dynamic viscosity of water. The proposed model aligns well with the numerically predicted drag coefficients for different oscillation periods and KC numbers, improving the underestimation of conventional model at $T = 3.5\,sec$.

A surge free decay simulation is conducted using engineering model with the proposed horizontal drag coefficient model. The configuration of the engineering model follows Otori et al. (2023). The initial displacement of $a_1 = 0.087\,m$ is used as the reference amplitude, and the

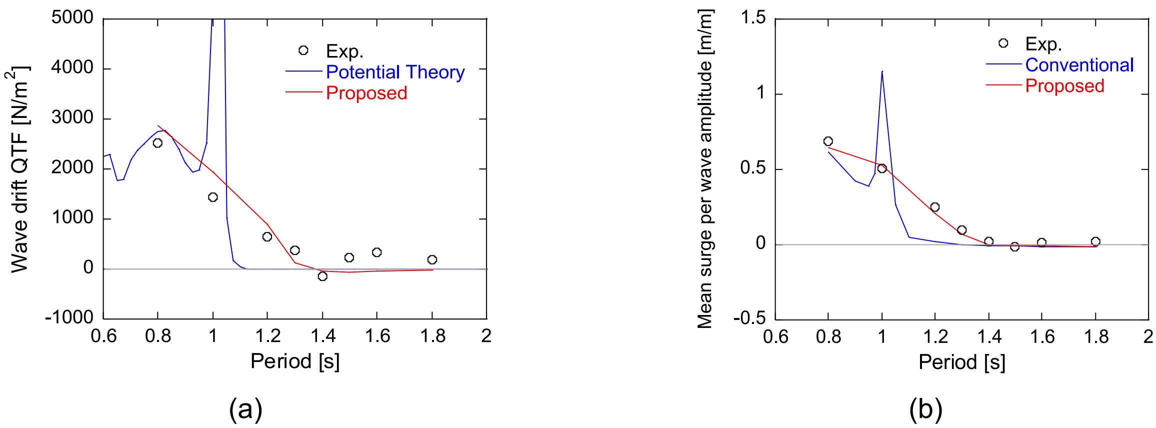

Fig. 18. Comparison of the results obtained from measurements, the QTF evaluated from potential theory, and the QTF evaluated from the numerical wave tank. (a) Surge wave drift QTF predicted by the potential theory and numerical water tank. (b) Mean surge displacement predicted by engineering model with wave drift QTF predicted by potential theory and numerical water tank.

surge natural period of $T = 3.5\ sec$ is used as the reference period for the normalization. C_{d11} is evaluated as 3.0 by the proposed model, while 1.4 by the conventional model. The predicted time series of surge free decay response is shown in Fig. 17. The prediction by the proposed model improves the agreement with the experiment compared to those by the conventional model.

3.3. Prediction of the wave drift QTF

To evaluate wave drift force QTFs without the use of costly water tank experiments, conventional models (e.g. Otori et al., 2023) have employed Newman's approximation based on the potential theory calculated by Ansys Aqwa (ANSYS Inc, 2019). The surge mean displacement predicted with the conventional model is shown in Fig. 18 (b). The conventional model overestimates the measurement by 126 % at the heave natural period of 1.0 s and underestimates the measurements at 1.2 s and 1.3 s.

To improve the prediction accuracy of the wave drift responses, the wave drift QTF is evaluated from the regular wave simulations of the numerical water tank. In this study, the wave drift QTF is evaluated as a mean component of hydrodynamic force on the floater in the surge direction. To evaluate the wave drift force without the nonlinear effect of mooring lines, linear springs are used to restrain floaters in studies such as Ikoma et al. (2021) and Seo et al. (2021). This study confirms that the catenary mooring system shows linear stiffness at 6.1 N/m in the surge direction, with less than 1 % variation across the surge displacements from −0.025 m to +0.025 m, which prevents surge drift force from being affected by the nonlinear response of mooring lines. For the validation, the wave drift QTF is also evaluated from the regular wave test of the water tank test.

The wave drift QTF obtained from the numerical regular wave simulation is compared to that evaluated from experiments and potential theory in Fig. 18 (a). The QTF obtained from the numerical water tank shows good agreement with the experimental results. Near the heave natural period of 1.0 s, the potential theory shows much larger value of wave drift QTF than that of experiment and the numerical water tank test, primarily because it neglects viscous damping on the heave motion (Molin and Lacaze, 2016; Tan et al., 2021). On the other hand, the QTF obtained from the numerical water tank at 1.0 s is 63 % lower than that from the potential theory. Furthermore, the numerical water tank results indicate larger values of the wave drift QTF at 1.2 s, where potential theory evaluates it to be zero.

Using the wave drift QTF obtained from numerical water tank, the dynamic analysis of floater in regular wave is conducted. The predicted surge mean displacement is presented in Fig. 18(b) and compared to the predictions using potential theory. The overestimation at the heave natural period of 1.0 s is improved and it is confirmed that evaluating wave drift QTF using the numerical water tank improves the prediction accuracy of the surge mean displacement in the engineering model.

3.4. Prediction of the surge-pitch coupling term of drag force

The surge amplitude predicted by engineering model underestimated the measurements less than 1.3 s of wave period as shown in Fig. 22 (Otori et al., 2023). To investigate this underestimation, the surge-pitch coupling term of drag force is investigated in this study. 6x6 global matrix of drag coefficients $[C_d]$ are presented as Eq. (18):

$$[C_d] = \begin{bmatrix} C_{d11} & 0 & 0 & 0 & C_{d15} & 0 \\ 0 & C_{d22} & 0 & C_{d24} & 0 & 0 \\ 0 & 0 & C_{d33} & 0 & 0 & 0 \\ 0 & C_{d42} & 0 & C_{d44} & 0 & 0 \\ C_{d51} & 0 & 0 & 0 & C_{d55} & 0 \\ 0 & 0 & 0 & 0 & 0 & C_{d66} \end{bmatrix} \tag{18}$$

where the subscript 1, 2, 3, 4, 5 and 6, representing the direction of surge, sway, heave, roll, pitch, and yaw directions.

The global matrix is evaluated using numerical water tank. C_{d11} and C_{d51} are evaluated through the surge forced oscillation, C_{d33} through the heave forced oscillation, and C_{d55} and C_{d15} through the pitch forced oscillation simulations. This study considers a symmetric motion in the Y-direction, so C_{d22}, C_{d44}, C_{d24}, C_{d42}, and C_{d66}, are not discussed in detail. Due to the symmetricity of the model, C_{d22}, C_{d44}, C_{d24}, and C_{d42} are regarded equal to C_{d11}, C_{d55}, $-C_{d15}$, and $-C_{d51}$, respectively. C_{d66} is not evaluated by the yaw forced oscillation simulations because it is out of scope in this study. The global drag matrix evaluated from the numerical forced oscillation simulations $[C_{d,CFD}]$ at $T = 1.2\ sec$, $a_1 = 0.01\ m$, $a_3 = 0.01\ m$, $a_5 = 3\ deg$ is evaluated as:

$$[C_{d,CFD}] = \begin{bmatrix} 7.25 & 0 & 0 & 0 & -11.12 & 0 \\ 0 & (7.25) & 0 & (11.12) & 0 & 0 \\ 0 & 0 & 21.82 & 0 & 0 & 0 \\ 0 & (6.36) & 0 & (17.86) & 0 & 0 \\ -6.36 & 0 & 0 & 0 & 17.86 & 0 \\ 0 & 0 & 0 & 0 & 0 & (C_{d66}) \end{bmatrix} \tag{19}$$

where the drag coefficients are obtained from drag force F_{D11}, F_{D33}, and F_{D15} and drag moment M_{D55} and M_{D51} in each direction as:

$$C_{d11} = \frac{F_{D11}}{-\frac{1}{2}\rho_w A|\dot{x}|\dot{x}}, C_{d33} = \frac{F_{D33}}{-\frac{1}{2}\rho_w A|\dot{z}|\dot{z}}, C_{d55} = \frac{M_{D55}}{-\frac{1}{2}\rho_w AR^3|\dot{\theta}|\dot{\theta}}, C_{d66} = \frac{M_{D66}}{-\frac{1}{2}\rho_w AR^3|\dot{\psi}|\dot{\psi}} \tag{20}$$

and the off-diagonal components as:

$$C_{d15} = \frac{F_{D15}}{-\frac{1}{2}\rho_w C_{d15}\, AR^2|\dot{\theta}|\dot{\theta}}, C_{d51} = \frac{M_{D51}}{-\frac{1}{2}\rho_w C_{d51}\, AR|\dot{x}|\dot{x}} \tag{21}$$

The global matrix of drag coefficients in the engineering model $[C_{d,eng}]$ conventionally evaluated from the distributed horizontal and vertical drag coefficients on Morison elements Otori et al. (2023) is obtained as Eq. (22):

$$[C_{d,eng}] = \begin{bmatrix} 7.32 & 0 & 0 & 0 & -1.35 & 0 \\ 0 & 7.32 & 0 & 1.35 & 0 & 0 \\ 0 & 0 & 22.82 & 0 & 0 & 0 \\ 0 & 2.83 & 0 & 16.80 & 0 & 0 \\ -2.83 & 0 & 0 & 0 & 16.80 & 0 \\ 0 & 0 & 0 & 0 & 0 & 2.42 \end{bmatrix} \tag{22}$$

where each component can be derived following the formulation by Ishihara and Zhang (2019) with modification of the pitch drag coefficient C_{d55} definition based on OrcaFlex (Orcina, 2020) as:

$$C_{d11} = \frac{1}{A_x}\sum_{i=1}^{N_w^{Corner}} C_{d_i}^{\,n} A_i^n; \quad C_{d33} = \frac{1}{A_z}\sum_{i=1}^{N_w^{Skirt}} C_{d_i}^{\,t} A_i^t;$$

$$\begin{aligned} C_{d55} = & \frac{1}{A_x R^3}\sum_{i=1}^{N_w^{Corner}} C_{d_i}^{\,n} A_i^n |z_{COR} - z_i|^3 \\ & + \frac{1}{A_z R^3}\sum_{i=1}^{N_w^{Skirt,Front/Rear}} C_{d_i}^{\,t} A_i^t x_i^2 \sqrt{x_i^2 + (z_{COR} - z_i)^2} \\ & + \frac{1}{A_z R^3}\sum_{i=1}^{N_w^{Skirt,Sides}} C_{d_i}^{\,t} A_i^t |x_i|^3; \end{aligned}$$

$$C_{d15} = -\frac{1}{A_x R^2}\sum_{i=1}^{N_w^{Corner}} C_{d_i}^{\,n} A_i^n (z_{COR} - z_i)^2; \; C_{d51} = -\frac{1}{A_x R}\sum_{i=1}^{N_w^{Corner}} C_{d_i}^{\,n} A_i^n (z_{COR} - z_i) \tag{23}$$

$C_{d_i}^{\,n}$ is the horizontal drag coefficient at the corner of the main body evaluated from the proposed hydrodynamic coefficient model of Eq. (17). $C_{d_i}^{\,t}$ is the vertical drag coefficients at the skirt evaluated from the model proposed by Otori et al. (2023). N_w^{Corner} is the number of elements in water at the corner of the main body representing the horizontal drag force. $N_w^{Skirt,Front/Rear}$ and $N_w^{Skirt,Sides}$ are the number of elements of the front/rear and side skirts, representing the vertical drag force. x_i, y_i, and z_i are the local coordinates for the element i in the distributed Morison elements of Otori et al. (2023). z_{COR} is the center of rotation in the forced oscillation. A_x and A_z are the characteristic area of the floater in the horizontal and vertical directions. A_i^n and A_i^t are the characteristic area of element i for the horizontal and vertical directions, respectively.

Comparing Eq. (19) and Eq. (22), $[C_{d,eng}]$ accurately predicts the diagonal components with an error of less than 6 %. However, it significantly underestimates the magnitude of the off-diagonal components, with errors of 88 % for C_{d15} and 56 % for C_{d51}. Fig. 19 illustrates the difference between the prediction by CFD and conventional engineering model method ΔC_{d15} and ΔC_{d51} across various oscillation periods. Here, ΔC_{d15} and ΔC_{d51} are defined as:

$$\Delta C_{d15} = C_{d15,CFD} - C_{d15,eng} \tag{24}$$

$$\Delta C_{d51} = C_{d51,CFD} - C_{d51,eng} \tag{25}$$

Both ΔC_{d15} and ΔC_{d51} shows a negative value, exhibiting a peak at the 1.0 s oscillation period.

To investigate the cause of the difference between the off-diagonal components of drag forces predicted by CFD and those evaluated from the horizontal and vertical drag coefficients, the dynamic pressure field during the pitch forced oscillation ($T = 1.2\,sec$; $a_5 = 5\,deg$) is visualized in Fig. 20 (a). In the pitch motion, vortices are observed at the edge of the skirts, which is the area enclosed by the dashed circle and is a dominant contributor to C_{d55} as indicated by Otori et al. (2023). It is found that the resultant low-pressure wake also interacts with the main body and creates a surge directional force; on the right side of the platform, the low-pressure wake affects the platform's side, while on the left side, the vortices are released under the skirt and the wake does not

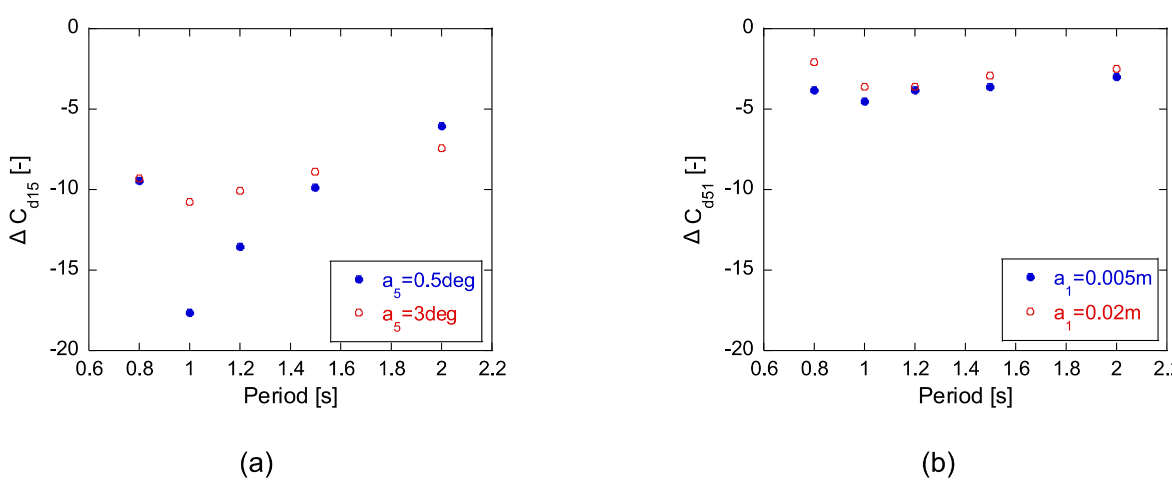

Fig. 19. Difference in surge-pitch coupling terms of drag coefficients: (a) $\Delta C_{d,15}$ and (b) $\Delta C_{d,51}$ predicted by CFD and those evaluated by distributed horizontal and vertical drag coefficients.

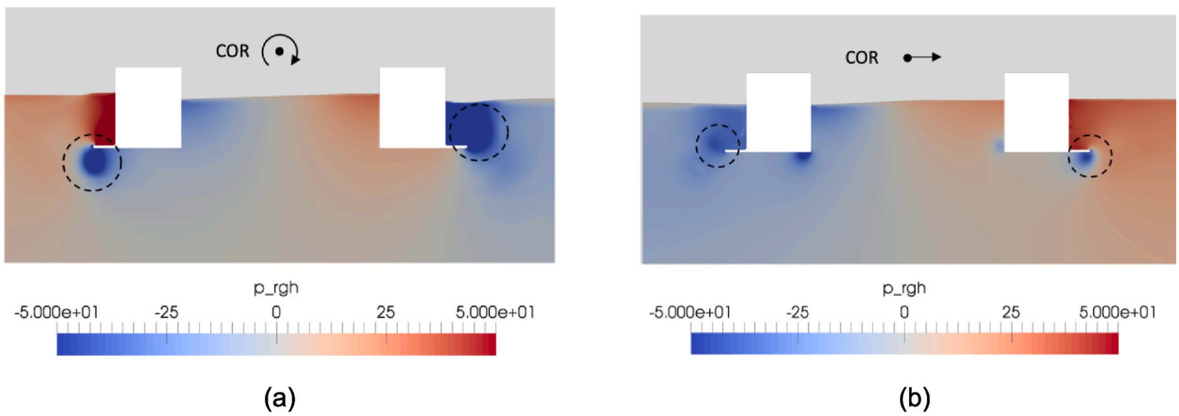

Fig. 20. Visualization of low-pressure wake at the skirt in the dynamic pressure field at maximum floater velocity. (a) Pitch oscillation ($T = 1.2\ sec$; $a_5 = 5\ deg$). (b) Surge oscillation ($T = 1.2\ sec$; $a_1 = 0.02\ m$). Z-X plane cross section at the center.

affect the platform's side. This results in a pressure difference between the platform's left and right sides, causing a positive force in the surge direction when $\dot{\theta} > 0$, corresponding the negative value of ΔC_{d15}. This flow distribution is unique to barge-type floater and therefore this coupling effect has not been included in the conventional formulation of Eq. (23) for semi-submersible floater, where only the surge drag force created by the flow normal to the corner of main body is considered for C_{d15}. The dynamic pressure in the surge forced oscillation ($T = 1.2\ sec$; $a_1 = 0.02\ m$) is also visualized in Fig. 20 (b). As enclosed by the dashed circle, vortices are observed at the edge of the skirt in the transverse direction of platform motion. This creates a positive drag moment in the pitch direction when $\dot{x} > 0$, corresponding the negative value of ΔC_{d51}. This coupling effect has also not been included in the conventional formulation of Eq. (23), where only the surge drag force created by the flow normal to the corner of main body is considered for C_{d51}.

To consider the influence of surge-pitch coupling terms on the dynamic response of barge-type floater, a new analysis procedure of engineering model is proposed. The off-diagonal terms are corrected according to the flowchart of dynamic analysis in Fig. 21. The surge and pitch coupling term of drag forces, ΔF_{d15} and ΔM_{d51} are approximated as:

$$\Delta F_{d15} = -\frac{1}{2}\rho_w \Delta C_{d15}\, AR^2 |\dot{\theta}_{Conv}| \dot{\theta}_{Conv} \tag{26}$$

$$\Delta M_{d51} = -\frac{1}{2}\rho_w \Delta C_{d51}\, AR |\dot{x}_{Conv}| \dot{x}_{Conv} \tag{27}$$

where, $\dot{x}_{Conv}$ and $\dot{\theta}_{Conv}$ are the surge velocity and pitch angular velocity evaluated from the time series of relative velocities at the edge of the front and rear skirts predicted by the conventional model as:

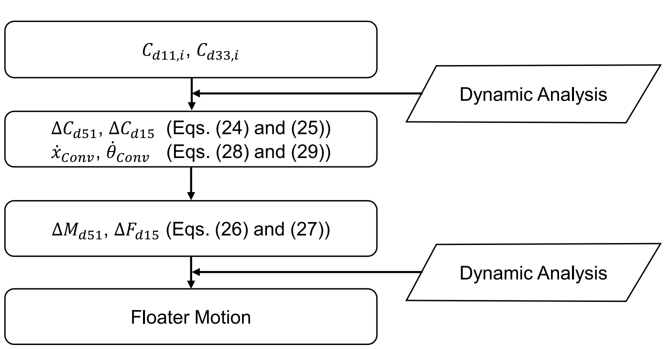

Fig. 21. Flowchart of predicting the floater motion using proposed correction method of off-diagonal terms.

$$\dot{x}_{Conv} = \frac{1}{2}\left(u_{r,Front} + u_{r,Rear}\right) \tag{28}$$

$$\dot{\theta}_{Conv} = \frac{1}{2R}\left(v_{r,Front} - v_{r,Rear}\right) \tag{29}$$

Here, $u_{r,Front}$ and $u_{r,Rear}$ are the surge relative velocity at the edge of the front and rear skirts, and $v_{r,Front}$ and $v_{r,Rear}$ are the heave relative velocity at the front and rear skirts. ΔC_{d15} and ΔC_{d51} are obtained in Fig. 19, corresponding to the oscillation period and amplitude. The reference oscillation periods and amplitudes are evaluated from the oscillation periods and amplitudes of $\dot{x}_{Conv}$ and $\dot{\theta}_{Conv}$. The amplitude dependence of ΔC_{d15} and ΔC_{d51} is linearly interpolated using the calculated values for two different amplitudes shown in Fig. 19. A is the representative area, defined as the area of skirts in X–Y plane of 0.0576 m^2.

Dynamic analysis with consideration of surge-pitch coupling drag term is then conducted by incorporating ΔF_{d15} and ΔM_{d51} into the equation of motion in the surge and pitch directions. The predicted RAOs by the proposed method are shown in Fig. 22. The prediction accuracy of surge amplitude is significantly improved by considering ΔF_{d15}, indicating that ΔF_{d15} contributes to the increase of surge amplitude for periods from 1.0 s to 1.3 s. The influence of considering ΔM_{d51} on the pitch motion is relatively small, but the underestimation by the conventional model at $T = 1.3\ sec$, close to the pitch natural period, is slightly improved. Considering the high accurate prediction by numerical water tank as shown in Fig. 12 (c), the prediction accuracy of the pitch amplitude near the natural period in engineering model needs to be further investigated in the future.

4. Conclusions

In this study, an applicability of numerical water tank for the dynamic response analysis of the barge-type floating platform is investigated. The conclusions are obtained as follows.

1. A numerical water tank is developed coupling with dynamic mooring model for barge-type floater. Wave excitation forces, free decay responses, and dynamic responses in regular waves predicted by numerical water tank show good agreement with experimental results.
2. It is clarified that the cause of the overestimation in measured normalized wave excitation force relative to that predicted by potential theory is the underestimation of the input wave height due to the interference of the reflected wave from the floater in the water tank test. By evaluating incoming waves without the platform simulated by numerical water tank, the normalized wave excitation forces show good agreement with those predicted by the potential theory.

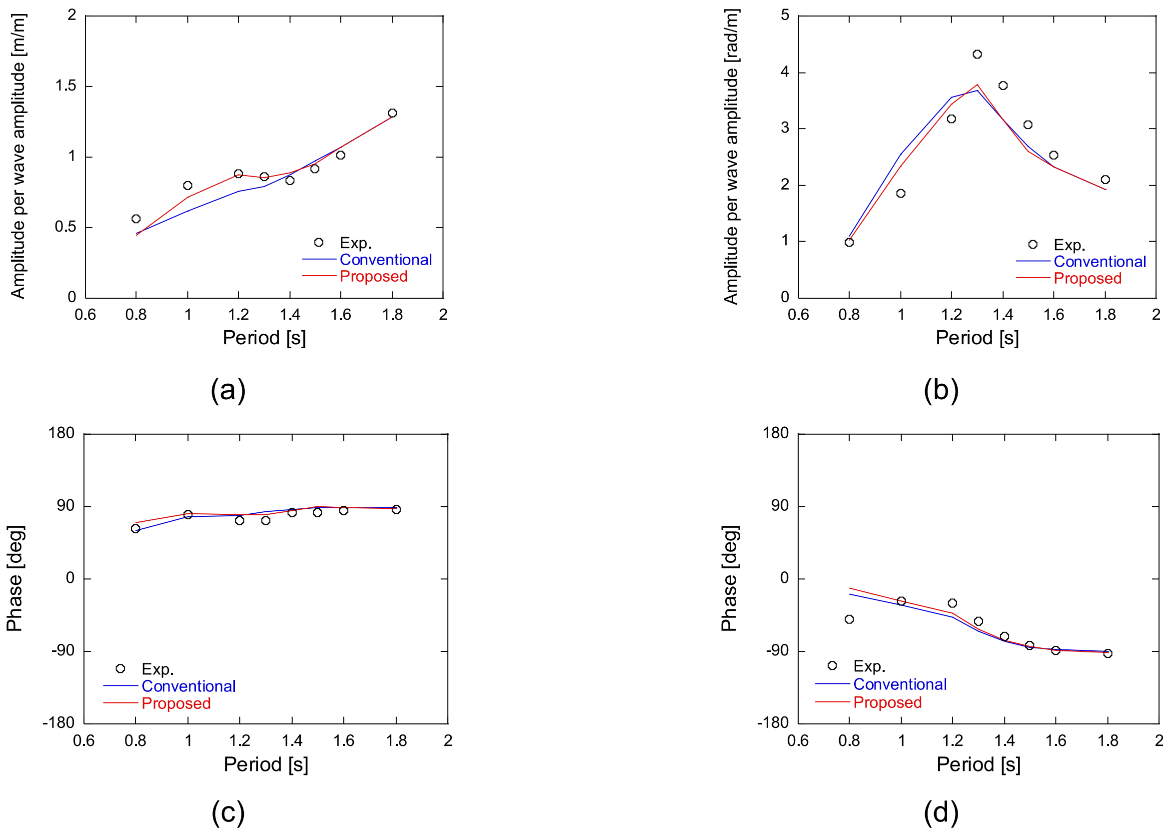

Fig. 22. Influence of surge-pitch coupling component of drag force on the dynamic response. Amplitudes in (a) surge and (b) pitch directions. Phases in (c) surge and (d) pitch directions.

3. A new drag coefficient model for the surge direction is proposed based on the drag coefficient obtained from numerical forced oscillation simulations at the surge natural period. By evaluating the horizontal drag coefficient from the proposed drag coefficient model, the prediction accuracy of engineering model is improved for the surge free decay motion.
4. The wave drift QTFs predicted by numerical water tank show good agreement with measurements compared to those predicted by potential theory, especially at the heave natural periods. The surge drift motion predicted by engineering model with the wave drift QTF predicted by numerical water tank show good agreement with measurements.
5. The surge-pitch coupling terms of drag force predicted by numerical water tank show the differences from those evaluated by distributed horizontal and vertical drag force on Morison elements due to the flow separation generated at thin skirt. The new engineering model analysis procedure is proposed to correct the surge-pitch coupling terms of drag force. The surge floater response predicted by the proposed engineering model shows good agreement with the measurements.

CRediT authorship contribution statement

Hiromasa Otori: Writing – original draft, Visualization, Validation, Software, Methodology, Investigation, Data curation, Conceptualization. **Yuka Kikuchi:** Writing – review & editing, Resources, Methodology, Funding acquisition, Conceptualization. **Irene Rivera-Arreba:** Writing – review & editing, Software, Conceptualization. **Axelle Viré:** Writing – review & editing, Resources, Conceptualization.

Declaration of competing interest

On behalf of my co-authors, I would like to declare that we have no known competing financial interests or personal relationships that could have appeared to influence the work reported in this manuscript entitled "***Applicability of numerical water tank for the dynamic response analysis of the barge-type floating platform***".

Acknowledgements

This research is supported by JSPS KAKENHI Grant Number JP23KJ0493. The water tank tests were carried in the Next Generation Floating Offshore Project funded by New Energy and Industrial Technology Development Organization. Viré is supported by the Dutch National Research Council (NWO) under the Talent Programme Vidi scheme (project number 19675). The authors wish to express their deepest gratitude to the concerned parties for their assistance during this study.

References

Akishima Laboratory, 2024. Small towing tank. https://akishima-labo.co.jp/en/facility/smalltowingtank/. (Accessed 14 July 2024).
Aliyar, S., 2022. Extreme Wave Interaction with Fixed and Floating Structures Using Hybrid Coupling Approach. École Centrale de Nantes & Indican Institute of Technology Madras. PhD thesis.
Aliyar, S., Ducrozet, G., Bouscasse, B., Bonnefoy, F., Sriram, V., Ferrant, P., 2022. Numerical coupling strategy using HOS-OpenFOAM-MoorDyn for OC3 Hywind SPAR type platform. Ocean Engineering 263, 112206. https://doi.org/10.1016/j.oceaneng.2022.112206.
ANSYS Inc., 2019. AQWA 2019 R1 [software].
Benitz, M.A., Schmidt, D.P., Lackner, M.A., Stewart, G.M., Jonkman, J., Robertson, A., 2014. Comparison of hydrodynamic load predictions between engineering models and computational fluid dynamics for the OC4-DeepCwind semi-submersible. Proceedings of the ASME 2014 33rd International Conference on Ocean. Offshore

and Arctic Engineering. https://doi.org/10.1115/OMAE2014-23985. V09BT09A006.
Berberović, E., van Hinsberg, N.P., Jakirlić, S., Roisman, I.V., Tropea, C., 2009. Drop impact onto a liquid layer of finite thickness: dynamics of the cavity evolution. Phys. Rev. E: Stat., Nonlinear, Soft Matter Phys. 79 https://doi.org/10.1103/PhysRevE.79.036306.
Beyer, F., Arnold, M., Cheng, P.W., 2013. Analysis of floating offshore wind turbine hydrodynamics using coupled CFD and multibody methods. In: Proceedings of the 23rd International Offshore and Polar Engineering Conference, Anchorage, Alaska, USA. June 30-July 5, 2013.
Beyer, F., Choisnet, T., Kretschmer, M., Cheng, P.W., 2015. Coupled MBS-CFD simulation of the IDEOL floating offshore wind turbine foundation compared to wave tank model test data. In: Proceedings of the 25th International Ocean and Polar Engineering Conference. Kona, Hawaii, USA. June 21-26, 2015.
Borisade, F., Choisnet, T., Cheng, P.W., 2016. Design study and full scale MBS-CFD simulation of the IDEOL floating offshore wind turbine foundation. J. Phys. Conf. 753 https://doi.org/10.1088/1742-6596/753/9/092002.
Borsboom, M., Jacobsen, N.G., 2021. A generating-absorbing boundary condition for dispersive waves. Int. J. Numer. Methods Fluids 93, 2443–2467. https://doi.org/10.1002/fld.4982.
Chen, H., Hall, M., 2022. CFD simulation of floating body motion with mooring dynamics: coupling MoorDyn with OpenFOAM. Appl. Ocean Res. 124, 103210 https://doi.org/10.1016/j.apor.2022.103210.
Davidson, J., Ringwood, J.V., 2017. Mathematical modelling of mooring systems for wave energy converters - a review. Energies 10 (5), 666. https://doi.org/10.3390/en10050666.
Eskilsson, C., Palm, J., 2022. High-fidelity modelling of moored marine structures: multi-component simulations and fluid-mooring coupling. J. Ocean Eng. Mar. Energy 8, 513–526. https://doi.org/10.1007/s40722-022-00263-w.
FLOATGEN, 2018. https://floatgen.eu/(accessed 3 May 2024).
Fukushima FORWARD, 2013. https://www.fukushima-forward.jp/english/index.html (accessed 3 May 2024).
Hall, M., Goupee, A., 2015. Validation of a lumped-mass mooring line model with DeepCwind semisubmersible model test data. Ocean Engineering 104, 590–603. https://doi.org/10.1016/j.oceaneng.2015.05.035.
Hirt, C.W., Nichols, B.D., 1981. Volume of Fluid (VOF) method for the dynamics of free boundaries. J. Comput. Phys. 39 (1), 201–225. https://doi.org/10.1016/0021-9991(81)90145-5.
Hywind Demo, 2009. https://www.equinor.com/news/archive/2009/09/08/InnovativePowerPlantOpened (accessed 3 May 2024).
Ikoma, T., Tan, L., Moritsu, S., Aida, Y., Masuda, K., 2021. Motion characteristics of a barge-type floating vertical-axis wind turbine with moonpools. Ocean Engineering 230, 109006. https://doi.org/10.1016/j.oceaneng.2021.109006.
Ishihara, T., Liu, Y., 2020. Dynamic response analysis of a semi-submersible floating wind turbine in combined wave and current conditions using advanced hydrodynamic models. Energies 13 (21), 5820. https://doi.org/10.3390/en13215820.
Ishihara, T., Zhang, S., 2019. Prediction of dynamic response of semi-submersible floating offshore wind turbine using augmented Morison's equation with frequency dependent hydrodynamic coefficients. Renew. Energy 131, 1186–1207. https://doi.org/10.1016/j.renene.2018.08.042.
Jacobsen, N.G., Fuhrman, D.R., Fredsoe, J., 2012. A wave generation toolbox for the open-source CFD library: OpenFOAM. Int. J. Numer. Meth. Fluids 70, 1073–1088. https://doi.org/10.1002/fld.2726.
Jiang, C., el Moctar, O., Schellin, T.E., 2021. Hydrodynamic sensitivity of moored and articulated multibody offshore structures in waves. J. Mar. Sci. Eng. 9 (9), 1028. https://doi.org/10.3390/jmse9091028.
Jonkman, J.M., 2007. Dynamics Modeling and Loads Analysis of an Offshore Floating Wind Turbine. National Renewable Energy Laboratory, Colorado, United States. https://doi.org/10.2172/921803. Technical Report NREL/TP-500-41958.
Kikuchi, Y., Ishihara, T., 2020. Comparison of dynamic response and levelized cost of energy on three floater concepts of floating offshore wind turbine systems. J. Phys. Conf. 1452, 012035 https://doi.org/10.1088/1742-6596/1452/1/012035.
Lee, S.C., Song, S., Park, S., 2021. Platform motions and mooring system coupled solver for a moored floating platform in a wave. Processes 9 (8), 1393. https://doi.org/10.3390/pr9081393.
Martin, T., Bihs, H., 2021. A numerical solution for modelling mooring dynamics, including bending and shearing effects, using a geometrically exact beam model. J. Mar. Sci. Eng. 9 (5), 486. https://doi.org/10.3390/jmse9050486.
Molin, B., Lacaze, J., 2016. On approximations of the wave drift forces acting on semi-submersible platforms with heave plates. Proceedings of the ASME 2016 35th International Conference on Ocean. Offshore and Arctic Engineering. https://doi.org/10.1115/OMAE2016-54166. V001T01A042.
NEDO floating offshore wind turbine technology guidebook. https://www.nedo.go.jp/content/100891410.pdf, 2018–. (Accessed 3 May 2024) (In Japanese).
NEDO Demonstration Project of Next-Generation Offshore Floating Wind Turbine, 2019. https://www.nedo.go.jp/floating/(accessed 3 May 2024).
Nematbakhsh, A., Bachynski, E.E., Gao, Z., Moan, T., 2015. Comparison of wave load effects on a TLP wind turbine by using computational fluid dynamics and potential flow theory approaches. Appl. Ocean Res. 53, 142–154. https://doi.org/10.1016/j.apor.2015.08.004.
Newman, J.N., 1974. Second-order, slowly-varying forces on vessels in irregular waves. In: Proceedings of the International Symposium on Dynamics of Marine Vehicles and Structures in Waves. London, UK, April 1-5, 1974.
Orcina Ltd., 2020. OrcaFlex release 11.2d [software]. www.orcina.com. (Accessed 3 May 2024).
Otori, H., Kikuchi, Y., Rivera-Arreba, I., Viré, A., 2023. Numerical study of hydrodynamic forces and dynamic response for barge type floating platform by computational fluid dynamics and engineering model. Ocean Engineering 284, 115100. https://doi.org/10.1016/j.oceaneng.2023.115100.
Otter, A., Murphy, J., Pakrashi, V., Robertson, A., Desmond, C., 2021. A review of modelling techniques for floating offshore wind turbines. Wind Energy 25 (5), 831–857. https://doi.org/10.1002/we.2701.
Palm, J., Eskilsson, C., Paredes, G.M., Bergdahl, L., 2016. Coupled mooring analysis for floating wave energy converters using CFD: formulation and validation. International Journal of Marine Energy 16, 83–99. https://doi.org/10.1016/j.ijome.2016.05.003.
Palm, J., Eskilsson, C., Bergdahl, L., 2017. An hp-adaptive discontinuous Galerkin method for modelling snap loads in mooring cables. Ocean Engineering 144, 266–276. https://doi.org/10.1016/j.oceaneng.2017.08.041.
Reddy, L.R., Viré, A., 2022. Numerical analysis of the semisubmersible using generating-absorbing boundary conditions. Proceedings of the ASME 2022 4th International Offshore Wind Technical Conference. https://doi.org/10.1115/IOWTC2022-98001. V001T01A003.
Rivera-Arreba, I., Bruinsma, N., Bachynski, E.E., Viré, A., Paulsen, B.T., Jacobsen, N.G., 2019. Modeling of a semisubmersible floating offshore wind platform in severe waves. J. Offshore Mech. Arctic Eng. 141 (6) https://doi.org/10.1115/1.4043942.
Robertson, A., Wang, L., 2021. OC6 Phase Ib: floating wind component experiment for difference-frequency hydrodynamic load validation. Energies 14 (19), 6417. https://doi.org/10.3390/en14196417.
Rusche, H., 2003. Computational Fluid Dynamics of Dispersed Two-phase Flows at High Phase Fractions. Imperial College London. PhD thesis.
Seo, M.G., Ha, Y.J., Nam, B.W., Kim, Y., 2021. Experimental and numerical analysis of wave drift force on KVLCC2 moving in Oblique waves. J. Mar. Sci. Eng. 9 (2), 136. https://doi.org/10.3390/jmse9020136.
Tan, L., Ikoma, T., Aida, Y., Masuda, K., 2021. Mean wave drift forces on a barge-type floating wind turbine platform with moonpools. J. Mar. Sci. Eng. 9 (7), 709. https://doi.org/10.3390/jmse9070709.
Thomsen, J.B., Ferri, F., Kofoed, J.P., 2017. Screening of available tools for dynamic mooring analysis of wave energy converters. Energies 10 (7), 853. https://doi.org/10.3390/en10070853.
Tran, T.T., Kim, D.H., 2015. The coupled dynamic response computation for a semi-submersible platform of floating offshore wind turbine. J. Wind Eng. Ind. Aerodyn. 147, 104–119. https://doi.org/10.1016/j.jweia.2015.09.016.
Tran, T.T., Kim, D.H., 2016. Fully coupled aero-hydrodynamic analysis of a semi-submersible FOWT using a dynamic fluid body interaction approach. Renew. Energy 92, 244–261. https://doi.org/10.1016/j.renene.2016.02.021.
Triantafyllou, M., Howell, C., 1994. Dynamic response of cables under negative tension: an ill-posed problem. J. Sound Vib. 173 (4), 433–447. https://doi.org/10.1006/jsvi.1994.1239.
Utsunomiya, T., 2016. Goto Island project. In: Cruz, J., Atcheson, M. (Eds.), Floating Offshore Wind Energy. Springer Cham, Cham, pp. 305–320. https://doi.org/10.1007/978-3-319-29398-1.
Wang, L., Robertson, A., Jonkman, J., Yu, Y.H., Koop, A., Borràs Nadal, A., Li, H., Bachynski-Polić, E., Pinguet, R., Shi, W., Zeng, X., Zhou, Y., Xiao, Q., Kumar, R., Sarlak, H., Ransley, E., Brown, S., Hann, M., Netzband, S., Wermbter, M., Méndez López, B., 2021. OC6 Phase Ib: validation of the CFD predictions of difference-frequency wave excitation on a FOWT semisubmersible. Ocean Engineering 241. https://doi.org/10.1016/j.oceaneng.2021.110026.
Weller, H.G., Tabor, G., Jasak, H., Fureby, C., 1998. A tensorial approach to computational continuum mechanics using object-oriented techniques. Comput. Phys. 12 (6), 620–631. https://doi.org/10.1063/1.168744.
WindFloat 1, 2009. https://www.principlepower.com/projects/windfloat1. (Accessed 3 May 2024).
Zhang, S., Ishihara, T., 2018. Numerical study of hydrodynamic coefficients of multiple heave plates by large eddy simulations with volume of fluid method. Ocean Engineering 163, 583–598. https://doi.org/10.1016/j.oceaneng.2018.03.060.